We are grateful to Drs. Keith Makinson and Hartmut Hellmer for their thorough and thoughtful reviews. This manuscript will be much improved by their input. We have made changes to our document and are including below an overview of these changes.

Referee comments are in **bold**, responses are in *italics*, and corrected grammar indicated by ~~strikethrough~~.

Hartmut Hellmer

Specific comments:

L032 – How can a paper published in 2006 cover the period 2002-2016? Actually, according to Monaghan et al. (2006), which covers the period 1955-2004, small changes in SA only occurred on the EAIS. *Thank you for pointing out this oversight. We have rewritten this text and provided an updated ref. (Wang et al., 2016).*

L055 – With regard to the direct flow of CDW into the ice shelf cavities of ABS Jenkins et al. (2010) is a more appropriate reference. *Corrected (L67). We have also added a cite to Jacobs et al. (2013), since Jenkins et al. (2010) only discusses measurements for Pine Island Glacier ice shelf, while Jacobs et al. (2013) demonstrates CDW flows into Getz (also ABS) as well.*

L081 – More precise: Hellmer et al. (2017) not just reversed the atmospheric conditions to a colder state but to 20th -century conditions. *We have augmented this section to include this clarification.*

L164 - ~~Equation (4) must read wb = QT0/L x rho~~. And, somewhere it should be mentioned that heat flux through the ice shelf is ignored. *Thank you for catching this typo! We have added a statement regarding the heat flux through the ice to the paragraph preceding Eqn. (1), and stated that we have ignored it for this study (reasonable for thick ice).*

L216 – It comes as a surprise that open ocean wct = h has a maximum value of 1914m, though the model domain (Fig. 1) only covers the southern Weddell Sea continental shelf. *Thanks. The value is now corrected, to 1211 m in Filchner Trough.*

L283 – It is not clear whether the 'bulk dye' was added to the whole water column or just to the surface-sigma layer. The confusion starts when looking at Fig. 8a, which looks more like a 'bottom dye' distribution. *The dye is added uniformly to all levels. We have amended the text to state "The bulk dye was initialized at a concentration of 100% <u>over the entire water column</u> but was not replenished after these simulations began.". We have included a couple of figures here to demonstrate the vertical structure of the bulk dye initialization (Figure 1) as well as the dye distribution in the surface and bottom layers.*
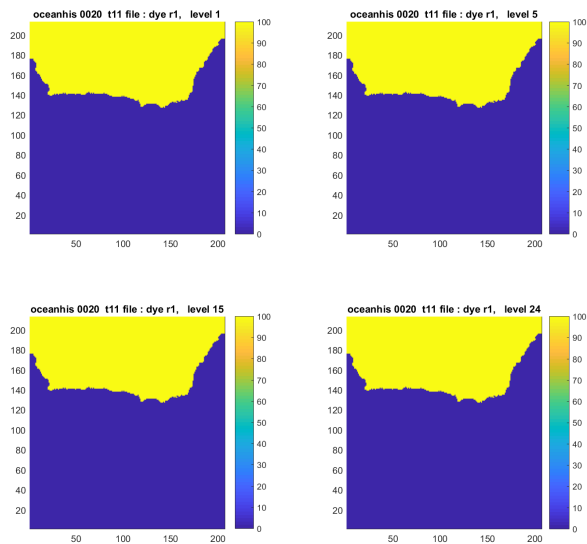
**Figure 1 Dye concentration from 0-100% in sigma levels 1 (bottom), 5, 15, and 24 (surface)**
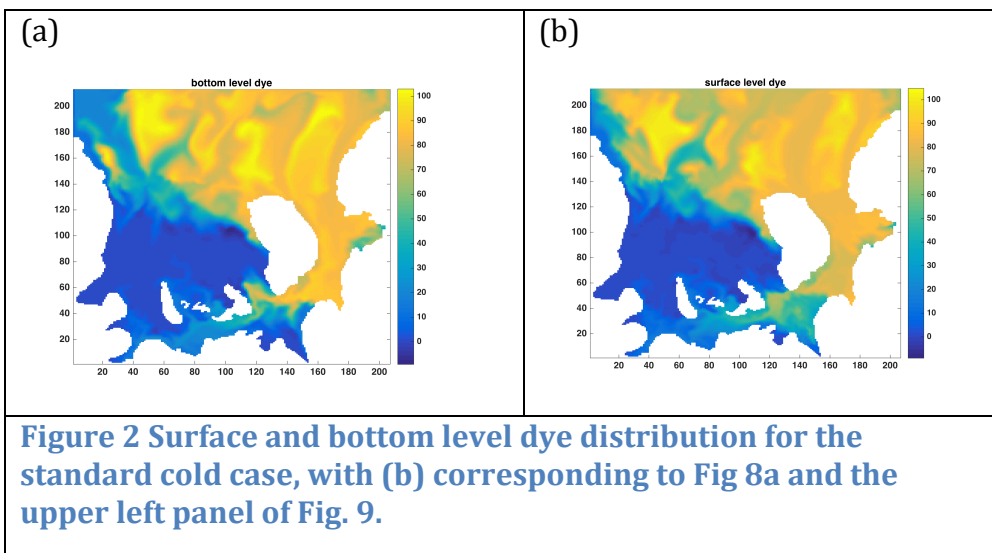
Figure 2 Surface and bottom level dye distribution for the standard cold case, with (b) corresponding to Fig 8a and the upper left panel of Fig. 9.

L305 – It is not clear what is meant with 'outer/interior grounding line' – please explain. *The labeling has been corrected using geographical referencing ("eastern", "southeastern", etc). We hope this helps to clarify the intended meaning.*

L335 – Here, a serious deficit of the model becomes obvious, since the refreezing along the eastern coast of Berkner Island (e.g., Rignot et al. (2013)) is missing, certainly because the model exaggerates the flow into the Filchner cavity. *We have clarified in the text how our lack of density gradient along the continental shelf yields a circulation bias with clockwise flow around Berkner Is., rather than the observed counterclockwise flow that is represented by models that include horizontal density gradients across the front.*

L396 – A reduction of area-averaged melt rates due to adding tides also happens for Support Force. *Support Force is now included in this statement.*

L426 – The comparison with Hellmer et al. (2012) is risky because this kind of circulation only happens for the 'warm phase', while here the same circulation pattern exists for the 'standard cold case'. Such comparison might provoke a critical reader to question ROMS' performance in general. *The intention of this phrasing was to highlight that in both these results and in the Hellmer et al. (2012) results the circulation within the FRIS cavity is clockwise, such that the primary ocean inflow is through FIS; but(!),we have decided to take a different approach in describing this circulation. The Discussion section now includes an overview of how our standard cold results are to be interpreted in the context of known present-day circulation. This addition also aims to address a comment by Keith Makinson.*

> Our results show that tide forcing is important to FRIS ice-ocean interactions over a range of initial temperatures and with large variations in regional impacts. The aim of these simulations was to apply, uniformly, temperatures and salinities that approximate (1) present-day, inflow conditions and (2) a representative temperature of future, inflow conditions, reflecting a modest increase in temperature; however, the circulation within this particular ice shelf cavity is strongly affected by sea-ice formation on top of a general circulation that establish an east to west density gradient across the continental shelf (e.g. Foldvik et al., 1985; Nicholls et al., 2009). As such, our "present-day" scenario is a hypothetical one that forms the basis of this sensitivity study but that should not be interpreted to reflect the known circulation within the cavity. The known circulation within the cavity, setup by the east to west density gradient on the continental shelf, has inflow in the Ronne Depression and a counter clockwise circulation around Berkner Is. (Foldvik et al. 2001). Our simulations for both the present-day and melt-adjusted cases predict inflow through the FIS and a clockwise circulation around Berkner Is. This pattern of circulation reflects the future warming scenario presented in Hellmer et al. (2012). This sensitivity study, therefore, does not include changes that would occur from a shift in cavity circulation from a scenario that has the east to west density gradient along the continental shelf to one where that density gradient is relaxed to the degree that the sub-ice-shelf cavity circulation would change. Although these simplifications restrict the predictive capacity of this study, they do not much affect the results of our sensitivity analysis on ice-ocean interactions within FRIS and in particular the feedbacks found between tides and changing geometry and implications for further research.

L714 – By summarizing important results I miss (5): The increase of refreezing in central RIS in the 'standard cold case', representing today's conditions. This is an important finding because refreezing in this area certainly changes the dynamics of the ice shelf by increasing the buttressing around Henry and Korff. *This result has already been reported in Makinson et al. (2011) for present-day ocean conditions; we therefore added the contribution of our work, with appropriate attribution to Keith Makinson for his, We clarified our results in the context of previous work by introducing a new Discussion section that focuses on basal freezing beneath FRIS (**Sect. 4.5**)*

4.5 Implications of regional freeze conditions on ice sheet mass balance

As described in **Sect. 3.2.1** and **Sect. 3.2.2**, refreezing occurs in our simulations throughout a large region of the central RIS. Refreezing in this region is qualitatively consistent with estimates of basal mass balance from satellite-based remote sensing (e.g., Joughin and Padman, 2003; Rignot et al., 2013; Moholdt et al., 2014). Persistent refreezing along ice flowlines can create a marine ice layer up to hundreds of meters thick, as observed in ice cores (Engelhardt and Determann, 1987; Oerter et al, 1992), and in radio-echo sounding and seismic measurements (Joughin and Vaughan, 2004; Lambrecht et al., 2007). These observations are important in the context of other studies which show that marine ice accretion supports ice shelf stability (Kulessa et al., 2014; McGrath et al., 2014; Li et al. (submitted)). Our standard cold tide-forced case produces local maxima in marine ice growth rates in the northwestern RIS, the region northeast and east of Korff Ice Rise, and the region to the north and west of Henry Ice Rise (**Fig. 5d**). The spatial pattern of these freeze conditions differs from observed patterns (Joughin and Padman, 2003; Rignot et al., 2013; Moholdt et al., 2014). We attribute this difference to the consequences of omitting the east to west density gradient along the continental shelf.

The regions of freezing are broadly consistent in all our model runs (**Fig. 5**) and the net mass increase in refreezing regions are increased when tide forcing is added (**Fig. 6**). Our standard cold tide-forced case has a ~4-fold mass gain compared to the standard cold no-tides case; this result is consistent with Makinson et al. (2011). In both warm cases, standard and modified geometry, adding tides increases net marine ice formation by a factor of two. That is, tides will continue to be important for marine ice accretion beneath FRIS if ocean temperatures rise as predicted by Hellmer et al. (2012, 2017) and will, therefore, continue to play a role in FRIS ice shelf stability.

We also included the following statement as (3) in our list of conclusions:

(3)   Adding tide forcing increases the overall freezing conditions for all three cases including the two warm cases. Since freeze conditions lead to marine ice accretion, and marine ice strengthens the ice shelf, the tidal contribution to ice-shelf dynamics is expected to continue through future ocean warming, increasing grounding and associated contact stresses in the region near the Henry and Korff ice rises and Doake Ice Rumples

L1044 – Please explain the difference between 'region' and 'inlet', used in Fig. 8. *We have corrected the use of "inlet" as shorthand for "inlet region" by changing "inlet" to "region", while also changing the parenthetical statement "*(see Fig. 4 for dye release regions)*" in order to make this phrasing consistent.*

L1061 – Please explain why Foundation shows a high dye concentration at the bottom. The signal cannot be advected from Support Force because there it does not exist, and highest

melting beneath Foundation should stabilize the water column such that most, if not all, of the dye should concentrate at the base. *We puzzled over this for a while. Based on the following figure (Fig. 3, below), and other analyses of T(z), S(z), and FIS dye profiles, we conclude that FIS dye is present at depth in the S. Channel due to the combined influence of mixing within the Möller inlet region as well as a shoaling of bathymetry in both Möller and South Channel. FIS dye appears to circulate first into the Möller inlet region where additional freshwater is added to the "upper" branch of FIS-doped water and where mixing processes transport dye to depths that correspond to bottom level depths within the South Channel. Within South Channel, all water contains meltwater from different sources, including locally. The density stratification depends on the sum of freshwater from all sources, whereas a specific dye (e.g., FIS), depends only on meltwater from that region.*

In order to clarify this influence, we have augmented section 4.3, to include the following statement:

> The presence of Foundation dye in the bottom level of the S. Channel transect reflects a shoaling of bathymetry (**Fig. 2c**) and mixing with the Möller region that allows the dye to be distributed to the bottom level within the Möller inlet region and then advected, at depth, through South Channel.

The evidence for this statement can be seen in Figure 3, below. Foundation dye is shown in the bottom, mid-depth and surface levels of the standard cold case. We attribute the circulation at this depth to be driven by changes in bathymetry, as shown in Fig. 2 of the main manuscript and here by w.c.t.
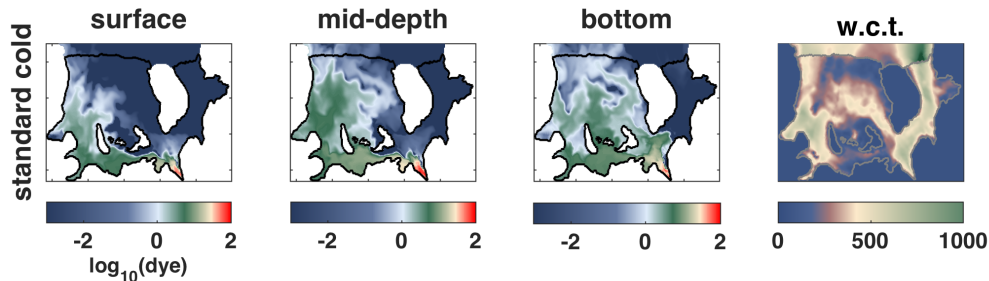

Figure 3: Maps of Foundation dye taken at the bottom level (N=1), a mid-depth level (N=15) and the surface level (N = 24) for the standard cold cases with water column thickness on right (as a duplicate of Fig. 2c, in main manuscript).

Technical corrections:

~~L031 – The dominant terms in the Antarctic ICE SHEET (AIS) mass budget....~~

~~L060 – We focus here ON . . .~~

~~L267 - . . . over the LAST 30 days?~~

~~L298 - . . . ice shelf frontal zone (ISFZ) of the RIS (here, front is redundant)~~

~~L337 - ...northWESTERN RIS.~~

~~L466 - . . . from all upstream sourceS.~~

L510 – Fig. 10e

L 833 – HelLmer, H. H.

L1000 - .. the extent of thE ice shelf...

L1017 – Locations of the six meltwater dye RELEASES. *We have included this change together with an emphasis on "model dye", which isn't really "released" per se, though we agree with this choice in verb.*

Keith Makinson

Suggested minor revisions:

~~L39 remove 'the'~~

~~L58 change to 'over the observational record.'~~

~~L60 change 'the' to 'on'~~

~~L69 remove both 'the'~~

~~L71 Modified Warm Deep Water (MWDW)?~~

~~L73 MWDW also seen at Ronne Ice Front (Mooring R2 and CTD's Foldvik et al 2001 doi:10.1029/2000JC000217)~~

~~L90 change to 'pattern and magnitude of'~~

L118 Are these temperatures and salinities restored throughout the model runs? *Yes. We have augmented the text to explain:* "Model hydrography is restored to these initial temperatures and salinity along the boundaries using a mixed radiation and nudging condition (Marchesiello *et al.*, 2001) over a 20-day period."

L122 It would be worth mentioning the lack of an east to west density gradient and hence the reverse circulation in the cavity. *We agree with the need to highlight this limitation in our model setup but feel that this information is best contained in the discussion section rather than the methodology section. We now use this information to introduce the discussion section and establish how our results can be interpreted in the context of other studies. The paragraph in question in our methodology section now reads:*

> Our simulations were initialized with a homogeneous, stationary ocean that has a potential temperature of either θ_{init} = -1.9°C ("cold case") or θ_{init} = -1.4°C ("warm case"). Initial salinity is defined as S_{init} = 34.65 for all cases. Model hydrography is restored to these initial temperatures and salinity at the boundaries using a mixed radiation and nudging condition (Marchesiello *et al.*, 2001) over a 20-day period. The standard geometry cold case incorporates a uniform temperature and salinity that approximates conditions of the primary water mass entering the ice shelf cavity (Foldvik et al., 2001; Nicholls et al., 2001, 2009). The consequences to FRIS cavity circulation in choosing a uniform θ_{init} and S_{init} are discussed in **Sect. 4**. The warm case represents a moderate ocean warming scenario with an increase of 0.5°C in the temperature of water being advected into the FRIS cavity. This change is much smaller than the 2°C temperature increase in the inflowing water by the end of this century predicted by Hellmer et al. (2012), but was chosen to investigate whether initial feedbacks due to melt-induced changes in cavity shape from initial warming might be positive or negative. Our idealized simulations do not include wind forcing, frazil ice, or sea-ice formation.

The intro to the discussion section (Sect. 4) goes into more details as follows.

Our results show that tide forcing is important to FRIS ice-ocean interactions over a range of initial temperatures and with large variations in regional impacts. The aim of these simulations was to apply temperatures and salinities that approximate (1) present-day inflow conditions and (2) a representative temperature of future inflow conditions, reflecting a modest increase in temperature. The choice of spatially constant initial temperature (θ_{init}) and salinity (S_{init}) does, however, influence circulation into and under the FRIS cavity. In the real ocean, spatial structure of the wind stress and production of dense HSSW by sea ice formation over Ronne Depression establishes an east-west density gradient across the continental shelf (e.g. Foldvik et al., 1985; Nicholls et al., 2009) that leads to stronger flows into the cavity across the RIS front than our model generates. Our "present-day" scenario should, therefore, be regarded as the basis of this sensitivity study rather than a prediction of known circulation within the cavity. In particular, our standard cold case misses the inflow in the Ronne Depression and a counter-clockwise circulation around Berkner Island (Foldvik et al. 2001). In contrast, our simulations for both the present-day and melt-adjusted cases predict the primary inflow through the FIS and a clockwise circulation around Berkner Island; this pattern of circulation is, however, consistent with the future warming scenario presented in Hellmer et al. (2012). The fundamental conclusions of our sensitivity analysis of ice-ocean interactions within FRIS are, however, independent of these differences from the real-world modern circulation.

L195-196 it would be useful to define what these numbers (Haney number and Beckmann and Haidvogel number), are if you are going to mention them.

The paragraph in question now includes the following description:

The ice draft and bathymetry were each smoothed to minimize errors in the baroclinic pressure gradient that arises with the terrain-following coordinate system used in ROMS (Beckmann and Haidvogel, 1993; Haney, 1991). The two parameters used to quantify smoothing are the Beckmann and Haidvogel number, rx0 = |h(e) − h(e')| / (h(e) + h(e')) (Beckmann and Haidvogel, 1993), and the Haney number, rx1 = |h(e, k) − h(e', k) + h(e, k-1) − h(e', k-1)| / (h(e, k) + h(e', k) − h(e, k-1) − h(e', k-1)) (Haney, 1991), where 1 ≤ k ≤ N and e and e' represent two adjacent cells. Together, these parameters establish that the surface (ice) and bottom bathymetry slopes are sufficiently small to reduce or eliminate spurious flows due to a horizontal pressure gradient and ensures hydrostatic consistency throughout the water column at adjacent horizontal grid nodes. Our Beckman and Haidvogel number, rx0, is less than 0.045 along both surface and bottom topographies, and our Haney number, rx1, is less than 10 in both surface and bottom levels except for some areas along the ice shelf front, where rx1 is larger and reaches a maximum value of 17.

L203 extreme stratification profile – a little more explanation maybe? *The sentence now reads: "*We initialized these models with horizontally uniform temperature and salinity fields taken from a standard warm case profile, in the vicinity north of Bjerkner Island, where the

strongest stratification of all runs is represented."

L212 Mention that this is a known problem/limitation with this type of model. *We have included this information.*

~~L216 1914 m. correct?~~

L233 .03 is this correct? Remove 'below'. *Yes. 0.03 is correct for the mode, but we agree that this number is a questionable asset to the discussion. We have changed the text to include information on the median: "…*and a median of 14 m*". A graphic of the distribution is included below.*

histogram of $\triangle zice = zice_m - zice_s$

Bin Count: 1.1e+04
Bin Center: 9.42
Bin Edges: [-Inf, 32.8]

Mode: 0.032684
Mean: 29.5562
Median: 14.1183
41% >20 m
17% >50 m
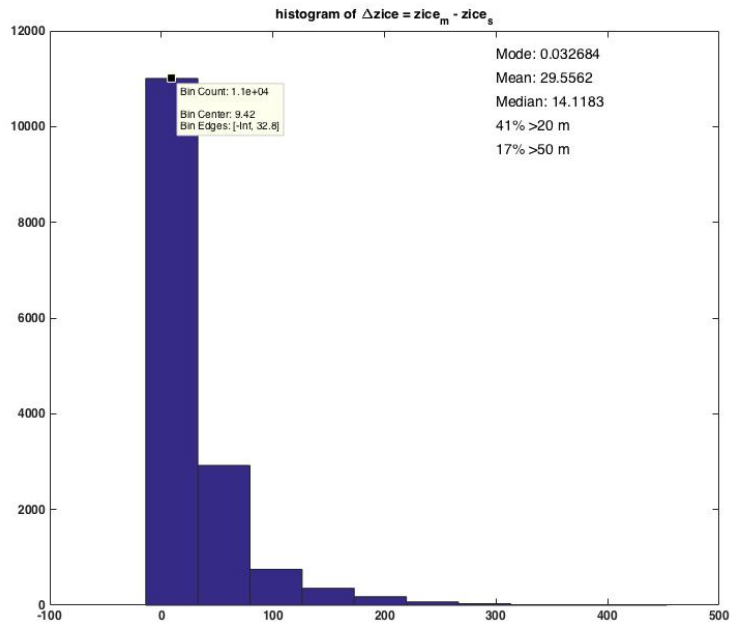
~~L234 remove 'above freezing'~~

~~L236 consider removing ',. Given. . ..bathymetry.'~~

~~L239-40 consider changing to 'conditions and ran with and without . . .'~~

~~L243 change to 'tide-resolving with at temporal resolution of 2 hours and'~~

~~L270 change 'over' to 'after'~~

L286 section label needed. *Indeed! We have corrected this and other Section label errors.*

~~L298 change to 'maximum tidal currents along'~~

Para L327-330 consider adding a value or percentage for the 'increased melt rates'

and 'slightly modifies'. *We have modified the text to read:*

> The pattern of w_b for the standard warm no-tides case (**Fig. 5b**) is generally similar to the standard cold no-tides case (**Fig. 5a**) but with a 3.5 fold increase in the shelf-averaged value. Changing cavity shape while imposing the same initial ocean

temperature in the modified warm case (**Fig. 5c**) only slightly reduces melt rates (by 10%) for the no-tides scenario (cf. **Fig. 5b and 5c**).

~~L336 it should be noted that there is very limited freezing north of Henry ice rise. L415 'southern' rather than 'innermost'~~

~~L441 'these' to 'the'~~

~~L466 sources~~

~~L510 Fig. 10e~~

~~L543 'is' to 'are'~~

~~L706 Ronne Ice Front~~

~~L759 Any bathymetry data from beneath ice shelves is useful as it will help better define the cavity geometry which you have demonstrated to be important for the whole system~~

~~(tides and circulation).~~

~~Fig 1. Add W and S labels for lon and lat.~~

~~L1010 remove 'than the standard geometry'~~

~~L1012 change to 'barotropic tidal transport'~~

~~L1017 change to 'continuous dye release'~~

~~Fig8 and 9. Mention in caption that this is after 2 years.~~

Fig12. Holland et al 2008 show similar melt figures over an extended range. doi:10.1175/2007jcli1909.1 *This is an important paper to cite here, and we have done so as follows: "*In general, our values are in range of those shown in Holland et al. (2008), (c.f. their Fig. 1 and our Fig. 12b),…."

Also Holland et al 2007 doi:10.1029/2006JC003915 show similar results to your dye tracer experiments. *We have included a reference to this important paper in the first paragraph of section 2.11: "*Our model excludes the influences of wind-driven circulation and sea-ice formation. As such, it is perhaps no surprise that these dye distributions are qualitatively similar to those shown by Holland et al. (2007)."

Tidal influences on a future evolution of the Filchner-Ronne Ice Shelf cavity in the Weddell Sea, Antarctica

Rachael D. Mueller[1], Tore Hattermann[2,3], Susan L. Howard[4], Laurence Padman[5],

[1]Earth & Space Research, Bellingham, WA 98225, USA

[2]Akvaplan-niva, Tromsø, 9296, Norway

[3]Alfred Wegener Institute, Helmholtz Centre for Polar and Marine Research, 27570 Bremerhaven, Germany

[4]Earth & Space Research, Seattle, WA 98121, USA

[5]Earth & Space Research, Corvallis, OR 97333, USA

Correspondence to: Rachael D. Mueller (mueller@esr.org)

Abstract. Recent modeling studies of ocean circulation in the southern Weddell Sea, Antarctica, project an increase over this century of ocean heat into the cavity beneath Filchner-Ronne Ice Shelf (FRIS). This increase in ocean heat would lead to more basal melting and a modification of the FRIS ice draft. The corresponding change in cavity shape will affect advective pathways and the spatial distribution of tidal currents, which play important roles in basal melting under FRIS. These feedbacks between heat flux, basal melting, and tides will affect the evolution of FRIS under the influence of a changing climate. We explore these feedbacks with a three-dimensional ocean model of the southern Weddell Sea that is forced by thermodynamic exchange beneath the ice shelf and tides along the open boundaries. Our results show regionally-dependent feedbacks that, in some areas, substantially modify the melt rates near the grounding lines of buttressed ice streams that flow into FRIS. These feedbacks are introduced by variations in meltwater production as well as the circulation of this meltwater within the FRIS cavity; they are influenced locally

by sensitivity of tidal currents to water column thickness and non-locally by changes in circulation pathways that transport an integrated history of mixing and meltwater entrainment along flow paths. Our results highlight the importance of including explicit tidal forcing in models of future mass loss from FRIS and from the adjacent grounded ice sheet as individual ice stream grounding zones experience different responses to warming of the ocean inflow.

1 Introduction

The dominant terms in the mass balance of the grounded portion of the Antarctic Ice Sheet are gains from snowfall and losses by gravity-driven flow of ice into the ocean. Around the ocean margins, the ice sheet thins sufficiently to float, forming ice shelves. Continuous gravity measurements from the GRACE satellite during 2002–2015 (Harig and Simons, 2015; Groh and Horwath, 2016) show that grounded-ice mass decreased during this period. This loss, which is a significant contribution to current rates of global sea level rise (e.g. Shepherd et al., 2012), is attributed to recent acceleration of ice loss (e.g. Harig and Simons, 2015), with little to no change in snowfall (Monaghan et al., 2006; Wang et al., 2016).

Most of this net mass loss is occurring in the Amundsen Sea sector (Sutterley et al., 2014), predominantly in glaciers flowing into Pine Island Bay (Mouginot et al., 2014; Khazendar et al., 2016), and is observed as glacier acceleration, ice-sheet thinning, and grounding-line retreat. Losses in this sector are correlated with observed thinning of the ice shelves (Pritchard et al., 2009, 2012), consistent with a reduction in back-stress ("buttressing") that impedes the seaward flow of the grounded ice (e.g., Scambos et al., 2004; Dupont and Alley, 2005; Rignot et al., 2014; Joughin et al., 2014). These studies demonstrate a need for improving predictions of how the extent and thickness of ice shelves will evolve as climate changes.

2

The mass budget for an ice shelf is the sum of mass gains from snow accumulation and advection of ice across the grounding line, and mass losses from iceberg calving, basal melting, surface runoff, and sublimation. Calving and melting each contribute roughly half of the total Antarctic Ice Sheet mass loss (Rignot et al., 2013; Depoorter et al., 2013), although this ratio varies substantially between ice shelves in different sectors. Surface runoff and sublimation are insignificant for most Antarctic ice shelves. The ice shelves that are currently experiencing the most rapid thinning are in the Amundsen and Bellingshausen seas where relatively warm Circumpolar Deep Water (CDW) has direct access into the ice shelf cavities (Jenkins and Jacobs, 2008; Padman et al., 2012; Jenkins et al., 2010b; Jacobs et al., 2013; Schmidtko et al., 2014). The large ice shelves in other sectors that are not directly influenced by CDW inflows are closer to steady state, suggesting that the transport of ocean heat under these ice shelves has not changed significantly over the observational record.

We focus here on Filchner-Ronne Ice Shelf (FRIS) in the southern Weddell Sea (**Fig. 1**). The FRIS is a large ice shelf ($\sim$430,000 km^2) that accounts for 30% of the total area of Antarctic ice shelves; however, it currently contributes only 10% of the total ice shelf mass loss. For comparison, Pine Island Glacier accounts for 0.4% of total area of Antarctic ice shelves but contributes 7% of total ice shelf mass loss (Rignot et al., 2013). The disproportionately small melt contribution from FRIS may change, however, in the coming century. Models suggest a large and persistent increase in ocean temperatures beneath FRIS in response to atmospheric changes in a warmer, future climate (Hellmer et al., 2012; Timmermann and Hellmer, 2013), and these conditions persisted even when atmospheric conditions were reversed to those of the 20$^{\text{th}}$ century (Hellmer et al., 2017). In the modern state, most of the water entering the ocean cavity under Filchner Ice Shelf (FIS) and Ronne Ice Shelf (RIS) is derived from High Salinity Shelf Water with a temperature close to the surface freezing point of -1.9°C (Nicholls et al., 2009). Traces of Modified Warm Deep

Water (MWDW) with temperature up to about -1.4°C are found in Filchner Trough near the FIS ice front (Darelius et al., 2016) and at the RIS front (Foldvik et al., 2001); however, MWDW does not appear to be a major heat source for melting beneath the ice shelf. In the warming scenarios of Hellmer et al. (2012), however, almost the entire FRIS cavity is flooded by WDW with above-zero temperatures by the end of the 21st century, leading tobasal melt rates an order of magnitude higher than present. In this warm state, the associated rapid thinning of the ice shelf would reduce the buttressing of the large marine-based grounded ice sheet surrounding FRIS (Ross et al., 2012), significantly accelerating future sea level rise (Mengel et al., 2016). Furthermore, simulations by Hellmer et al. (2017) show that the increased meltwater production will sustain the warm inflow even if atmospheric conditions were reversed to a colder state, suggesting the existence of an irreversible tipping point once melting increases past a certain threshold.

These estimates of increased melt, however, assume that cavity geometry does not change in a way that alters the access of ocean heat to the FRIS base. Studies of Larsen C Ice Shelf (Mueller et al., 2012) and Pine Island Glacier ice shelf (Schodlok et al., 2012) showed that changes to the ice shelf cavity shape can significantly alter the spatial pattern of basal melt rate, particularly in regions where tidal currents contribute substantially to the total turbulent kinetic energy near the ice base. Tides were not explicitly included in the forcing for the Hellmer et al. (2012) study. However, tidal currents often play a critical role in setting the pattern and magnitude of basal melt rates under cold water ice shelves (MacAyeal, 1984; Padman et al., in press) including FRIS (Makinson et al., 2011), which leads us to hypothesize that tides would influence changes in meltwater production from a warming ocean.

We explore this hypothesis using a suite of numerical model simulations that incorporate variations in tide forcing, initial temperature, and cavity geometry together with thermohaline interactions at the interface between the ocean and ice shelf. We then use these

100   models to describe how feedbacks between ice shelf thinning and predicted tidal currents in

101   the ice shelf cavity influence the evolution of a tide-dominated ice shelf environment under

102   the condition of increased influx of ocean heat. Lastly, we consider the role of tides on basal

103   mass loss near the grounding lines of each of the major ice streams supplying ice to FRIS, as

104   a guide to how individual ice stream grounding zones might respond to the projected

105   increase in ocean heat flux to the FRIS cavity.

106   **2 Methods**

107   **2.1 Model overview and thermodynamic parameterization**

108   Our simulations were carried out with a version of the Regional Ocean Modeling System

109   (ROMS 3.6; Shchepetkin and McWilliams, 2009) that has been modified to include

110   pressure, friction, and surface fluxes of heat and salt imposed at the base of the ice shelf

111   (Dinniman et al., 2007, 2011; McPhee et al., 2008; Mueller et al., 2012). ROMS is a

112   hydrostatic, 3D primitive equation model with a terrain-following (σ-level) coordinate

113   system and Arakawa-C staggered grid. Our model domain (**Fig. 1**) covers a portion of the

114   southern Weddell Sea, Antarctica including FRIS. The grid spacing is 5 km with $N = 24$

115   vertical levels. A full description of model parameter choices and processing options is

116   given in a supplementary document.

117   Two model geometries were used in our set of simulations, one representing the modern

118   state (standard geometry) and the other representing a possible future state (modified

119   geometry). Model geometry consists of a land mask (including grounded ice sheet), seabed

120   bathymetry (h), and ice draft (z_{ice}). These grids are described in **Sect. 2.2**.

121   Our simulations were initialized with a homogeneous, stationary ocean that has a

122   potential temperature of either $\theta_{init} = -1.9°C$ ("cold case") or $\theta_{init} = -1.4°C$ ("warm case").

123   Initial salinity was set as $S_{init} = 34.65$ for all cases. Model hydrography was restored to θ_{init}

5

Circulation develops through buoyancy forcing caused by thermodynamic exchange at the base of the ice shelves and, for tide-forced cases, by boundary conditions of tidal depth-integrated velocity and sea surface height. The thermodynamically-driven component of the circulation was introduced by scalar fluxes at the ice-ocean interface beneath FRIS. These fluxes are based on a simplified version of the 3-equation parameterization that assumes that the heat flux through the ice shelf is negligible (Hellmer and Olbers, 1989; Holland and Jenkins, 1999):

$$Q_T^o = \rho_o c_{po}(\alpha_h u_* + m)\Delta T \text{ [W m}^{-2}\text{]}, \tag{1}$$

$$Q_S^o = \rho_o(\alpha_s u_* + m)\Delta S \text{ [kg m}^2\text{ s], and} \tag{2}$$

$$T_b = T_f = 0.0939 - 0.057S_b + 7.6410\times10^{-4}z_{ice} \text{ [°C]}. \tag{3}$$

In Eq. (1), the surface heat flux (Q_T^o) is determined by the combined effect of thermal forcing and turbulent heat exchange. The thermal forcing is represented as $\Delta T = (T_b - T_o)$, where T_b is the temperature at the ice-ocean interface and T_o is the temperature of the ocean mixed layer under the ice base. The value of T_b is assumed to be the freezing point temperature, T_f, and depends on the salinity at the ice-ocean interface, S_b, as well as the ice draft, $z_{ice} < 0$

6

147   (Foldvik and Kvinge, 1974; Dinniman et al., 2007). For T_o, we follow a common approach

148   of using the temperature of the surface σ-layer in place of mixed layer values, with the

149   thickness of the surface σ-layer beneath the ice shelf cavity in our standard grid ranging

150   from 2 to 24 m and with 72% of points between 5 and 15 m. The turbulent heat exchange at

151   the ice-ocean interface is represented by a thermal transfer coefficient, α_h, scaled by a

152   friction velocity, u_*. This turbulent heat exchange is then adjusted by a meltwater advection

153   term, m, that corrects the scalar fluxes for a computational drift that is introduced as an

154   artifact of assumptions made in the numerical representation of the ice shelf as a material

155   boundary (Jenkins et al., 2001). We define $m = -\alpha_s u_* (1 - S_o/S_b)$ where $S_b < 5$, and $m = 0$

156   elsewhere. The friction velocity is calculated from the surface quadratic stress of the upper

157   sigma level as $u_* = C_d^{1/2}|\mathbf{u}|$, where $C_d = 2.5 \times 10^{-3}$ is a constant drag coefficient and $|\mathbf{u}|$ is

158   the magnitude of the surface layer current. The potential density of seawater, $\rho_o(x, y, z, t)$, is

159   evaluated for the uppermost layer, with the heat capacity of the ocean, c_{po}, assumed constant

160   at 3985 J kg^{-1} °C^{-1}. ΔS is the salinity equivalent to ΔT and is defined as $\Delta S = (S_b - S_o)$,

161   with S_b solved by quadratic formula from combining Eq. 1, 2, and 3 (without the meltwater

162   advection term, m) and S_o representing the salinity of the surface σ-layer.

163   These heat and salt fluxes (Q_T^o, Q_S^o) depend on scalar transfer coefficients (α_h, α_s) that are

164   proportional to each other by a "double diffusive" parameter, $R = \alpha_h/\alpha_s$ (McPhee et al.,

165   2008). Chapter 2 in Mueller (2014) provides a more detailed explanation of the background

166   and motivation for this parameterization. Here, we used scalar transfer coefficients based on

167   observations of the RIS sub-ice-shelf cavity (Jenkins et al., 2010a), with $\alpha_h = 1.1 \times 10^{-2}$ and

168    $R = 35.5$. The meltwater-equivalent melt rate term is derived by scaling the heat flux, Q_o^T, by

169   latent heat, $L = 3.34 \times 10^5$ J kg^{-1}, and the density of ice, $\rho_i = 918$ kg m^{-3}, such that

170

171    $w_b = -Q_o^T/(L\,\rho_i)$ [m s^{-1}].   (4)

172   Melting ice is indicated by $w_b > 0$ and represents the thickness of freshwater added to the

173   ocean surface, per second. These equations highlight that basal melting is driven by ocean

174   heat and motion, the latter being influenced by thermohaline circulation and tides.

175   A set of 12 model simulations was performed and is summarized in Table 1. A detailed

176   description of the different simulations is given in **Sect. 2.3**. Each case involves a

177   combination of standard or modified geometry, cold or warm ocean, and tidal forcing

178   switched off or on. For tide-forced simulations, tide heights and barotropic currents were

179   specified along the domain's open-ocean boundaries (see **Fig. 1**). The tidal boundary

180   conditions were obtained for the four most energetic tidal constituents $(K_1, O_1, M_2,$ and $S_2)$

181   from the CATS2008 barotropic inverse tide model, an updated version of the circum-

182   Antarctic model described by Padman et al. (2002). These four constituents account for 94%

183   of the total tidal kinetic energy for this region, based on CATS2008 estimates. Flather

184   (1976) boundary conditions were used for the barotropic velocity with free surface

185   conditions following Chapman (1985). Radiation conditions for baroclinic velocities were

186   applied following Raymond and Kuo (1984). Tracer equations were radiated across the open

187   boundaries (Marchesiello et al., 2001) and nudged to initial conditions over a 20-day time

188   scale.

189   **2.2 Geometries**

190   The grid of seabed bathymetry (h) over the entire domain (**Fig. 2a**) was derived from the

191   RTOPO-1 gridded dataset (Timmerman et al., 2010). The ice shelf is represented by a non-

192   evolving, although freely floating, surface boundary based on an ice draft (z_{ice}, **Fig. 2b**) that

193   was also derived from RTOPO-1. The land mask was adjusted around the ice rises and

194   rumples in the southern RIS to follow the grounding line provided by Moholdt et al. (2014).

195   Values of h and z_{ice} in regions of the ice sheet that are grounded in the RTOPO-1 mask but

196   floating (i.e., ice shelf) in the mask obtained from the Moholdt et al. (2014) data were

197   computed by linear interpolation and a nearest-neighbor extrapolation to ice shelf points in

198   the original RTOPO-1 grids.

199   The ice draft and bathymetry were each smoothed to minimize errors in the baroclinic

200   pressure gradient that arises with the terrain-following coordinate system used in ROMS

201   (Beckmann and Haidvogel, 1993; Haney, 1991). The two parameters used to quantify

202   smoothing are the Beckmann and Haidvogel number, $rx0 = |h(e) - h(e')| / (h(e) + h(e'))$

203   (Beckmann and Haidvogel, 1993), and the Haney number, $rx1 = |h(e, k) - h(e', k) + h(e, k-1) - h(e', k-1)| / (h(e, k) + h(e', k) - h(e, k-1) - h(e', k-1))$ (Haney, 1991), where $1 \leq k \leq N$

204

205   and e and e' represent two adjacent cells. Together, these parameters establish that the

206   surface (ice) and bottom bathymetry slopes are sufficiently small to reduce or eliminate

207   spurious flows due to a horizontal pressure gradient and ensures hydrostatic consistency

208   throughout the water column at adjacent horizontal grid nodes. Our Beckman and Haidvogel

209   number, rx0, is less than 0.045 along both surface and bottom topographies, and our Haney

210   number, rx1, is less than 10 in both surface and bottom levels except for some areas along

211   the ice shelf front, where rx1 is larger and reaches a maximum value of 17.

212   Our maximum values of rx1 are larger than typically recommended for ROMS. To test

213   whether large values lead to significant circulation from resulting errors in the baroclinic

214   pressure gradient, we ran unforced models for each of the standard and modified grids. We

215   initialized these models with horizontally uniform temperature and salinity fields, using an

216   extreme density profile in order to get an upper bound on the grid errors. We chose a profile

217   from a location just north of the eastern side of Berkner Island. The T and S profiles in this

218   region yielded a relatively large pycnocline with potential density changing from 1027.67 to

219   1027.77 kg m^{-3} between 0 and 400 m, a depth range where the change in ice draft along the

220   ice shelf front is most likely to cause spurious flows. This profile was extrapolated in depth

221   and horizontally to yield the uniformly stratified test hydrography. The resulting velocities in

222   these unforced runs are representative of maximum grid errors that may occur in the full

223 simulations. We quantified grid error by comparing the currents generated by these
224 uniformly stratified, unforced model runs to the 30-day averaged current speeds in the
225 standard warm tide-forced and modified warm tide-forced cases. The maximum fractional
226 error in our velocity fields is 10% for the standard grid and 5% for the modified grid. Large
227 errors were limited to a very small region north and northwest of Berkner Island; the relative
228 error over most of the domain is negligible.

229 In the smoothed standard geometry, the ice draft beneath FRIS ranges from 1537 m at
230 the deepest part of the grounding line to 11 m at the shallowest point of the ice shelf front.
231 Small values of ice draft near the ice front are unrealistic, but are a consequence of necessary
232 smoothing in models that use terrain-following vertical coordinates. The region of thinned
233 ice shelf represented by these small values is a narrow band along the ice front (**Fig. 2b and**
234 **2c**). The water column thickness, $wct = h + z_{ice}$, ranges from 50 m (a specified minimum
235 value, chosen for numerical stability) to 1111 m under FRIS. In the open ocean, $wct = h$ and
236 has a maximum value of 1211 m, in the Filchner Trough.

237 Using this standard geometry, we conducted simulations for both the cold and warm
238 cases described in **Sect. 2.1**, with and without tides. The modified geometry was then
239 created from the output of the two 20-year tide-forced simulations of the standard cold and
240 standard warm cases (see **Sect. 2.3.2**). In creating this grid, we assumed that the RIS and FIS
241 are both in steady state under present-day conditions (Rignot et al., 2013; Depoorter et al.,
242 2013; Moholdt et al., 2014) represented by our standard cold case, and that the most accurate
243 simulations of basal melting will be those with tidal forcing included (Makinson et al.,
244 2011). Steady state requires that mass input from lateral ice transport across the grounding
245 line plus snowfall onto the ice shelf is balanced by basal melting and iceberg calving that
246 maintains a constant ice-front position. The difference in local melt between the standard
247 warm and standard cold cases, neglecting any ice dynamical feedbacks, would then be

248 equivalent to the rate of change in thickness of the ice shelf, provided the change in melt rate

249 is not offset by changes in mass inputs to the ice shelf.

250 We applied the melt-rate imbalance for a period of 50 years to provide a sufficiently

251 large change in z_{ice} to significantly alter the general circulation and tidal currents in the

252 cavity. The resulting modified geometry thins z_{ice} by an average across the ice shelf of 30 m

253 and a median of 14 m. The ice shelf thickens in the freezing (mid-shelf) regions by a

254 maximum of 14 m and thins in the melt regions by a maximum of 453 m, although about

255 99% of all thinning values are less than 200 m (**Fig. 2c and 2d**). The combined area where

256 the ice shelf thickens is only 0.1% of the total ice shelf area and is characterized by an

257 average increase of 5 m. The modified-case bathymetry is the same as the standard case

258 bathymetry, so these changes in z_{ice} cause an equal magnitude change in *wct*. We chose to

259 only run the modified geometry as a warm case because it is designed to represent the FRIS

260 cavity under warm conditions, with and without the influence of tidal forcing along the open

261 boundaries.

262 **2.3 Model Simulations**

263 Three types of simulations were run: (1) tide-resolving with time-averaged output every two

264 hours and no thermodynamic exchange; (2) simulations with ice/ocean thermodynamics,

265 with and without tide forcing; and (3) passive dye tracer simulations to explore circulation

266 patterns. These runs are more fully described in the following sections.

267 **2.3.1   Tide-resolving simulations with no thermodynamic exchange**

268 We performed two 40-day simulations with 2-hr-averaged output, one with standard

269 geometry and the other with modified geometry, to predict tidal current speeds. These

270 simulations ("tides-only cases") did not include thermodynamic interactions at the ice-ocean

271 boundary, so that the ocean remained unstratified at its initial homogeneous state. Absent

11

272   stratification, the resulting currents are barotropic in nature, although some depth-

273   dependence arises from the friction at the seabed and ice base (see, e.g., Makinson et al.,

274   2006).

275   The spatial characteristics of time-averaged tidal currents (**Fig. 3a,b**) were calculated as

276   the time- and depth-averaged tidal current speed $|\mathbf{u}|_{tide}$, given by:

277

278    $$|\mathbf{u}|_{tide} = \langle\sqrt{u_b^2 + v_b^2}\rangle_t \ \ [\text{m s}^{-1}], \tag{5}$$

279

280   where $u_b(x,y,t)$ and $v_b(x,y,t)$ are orthogonal components of modeled, depth-averaged

281   current and $\langle\ \rangle_t$ represents temporal averaging over the last $t = 30$ days of the model run,

282   which characterizes two cycles of the 15-day spring-neap cycles generated by the M_2, S_2, K_1,

283   and O_1 tides. The maximum tidal speed at spring tides is, typically, about $2\times|\mathbf{u}|_{tide}$.

2.3.2 Base simulations

285   Six simulations, each 20-30 years long, were conducted with thermodynamic exchanges of

286   heat and freshwater at the ocean/ice-shelf interface. Output for each of these simulations was

287   averaged over the last 30 days. Three of these were run with tidal forcing, two standard

288   geometry cases, one with $\theta_{init} = $ -1.9°C (cold) and one with $\theta_{init} = $ -1.4°C (warm), and one

289   modified geometry case with $\theta_{init} = $ -1.4°C (warm). We refer to these runs as: standard cold

290   tide-forced, standard warm tide-forced, and modified warm tide-forced (**Table 1**). These

291   three simulations all reached steady state solutions by 20 years. We then used the last 30-day

292   averaged output grids in these tide-forced solutions as initial conditions for three "restart"

293   simulations without tidal forcing, each of which reached a new steady state over 10 model

294   years. We refer to these runs as: standard cold no-tides, standard warm no-tides, and

295   modified warm no-tides.

2.3.3 Passive dye tracer simulations

Three simulations were run with passive dye tracers to investigate the advection and diffusion of water from different regions. These simulations were initialized with the steady-state solutions of the standard cold, standard warm, and modified warm tide-forced cases. They were run for 2 years each, with 30-day averaged output. Two types of dyes were used. Passive "meltwater" dyes were continuously added to the model's surface sigma layer at a rate of $1\text{x}10^4 w_b$ in six regions, the grounding zones of five tributary glaciers plus "South Channel", the region of ice shelf south of Henry Ice Rise (**Fig. 4**). A "bulk" dye was added to the open ocean region shown in **Fig. 4.** The bulk dye was initialized at a concentration of 100%, over the entire water column, but was not replenished after these simulations began.

3 Results

The main result of our study is that melt-induced changes in cavity shape introduce regional variations in tide current speeds and advection pathways that result in spatial variations in feedbacks to basal melting. We explain these insights in the following subsections through analyses of: tidal currents, spatial patterns of w_b, ice-shelf-averaged w_b and its sensitivity to model setup, regionally-averaged w_b and its sensitivity to model setup, and ocean circulation patterns shown by maps of dye tracer distribution.

3.1 Tidal currents in tide-resolving simulations

The maps of $|\mathbf{u}|_{tide}$ defined by **Eq. (5)** (**Fig. 3a and 3b**) highlight the spatial variability of tidal currents beneath FRIS. In particular, they show negligible tidal currents in the inlets of the major ice streams that feed into the RIS and FIS, and local maxima along the northeastern RIS front and South Channel.

The maximum tidal currents along the northeastern ice shelf frontal zone of the RIS are consistent with previous tide models (e.g., Robertson et al., 1998; Makinson and Nicholls,

320 1999). This region has a relatively small *wct* (**Fig. 2c**), so a larger tidal current here is
321 expected. The melt-induced geometry change in the modified case (**Fig. 3c**) has the overall
322 effect of increasing the water depth in this region and reducing these tidal currents (**Fig. 3d**).

323   Tidal currents in South Channel are not as strong as those in the northeastern ice shelf
324 frontal zone, but the melt-induced change in *wct* and $|\mathbf{u}|_{tide}$ is larger than in that region (**Fig.**
325 **3c and 3d**). The melt-induced change in *wct* is also large along the southeastern grounding
326 line of FIS (**Fig. 3c**). These changes in *wct* and $|\mathbf{u}|_{tide}$ enhance barotropic tidal transport
327 $(|\mathbf{u}|_{tide} \times wct)$ along the southern edge of South Channel, the eastern grounding line of FIS,
328 and along the northeast boundary of RIS with Berkner Island (**Fig. 3e**). These comparisons
329 show that melt-induced ice shelf thinning generally reduces the local tidal currents (**Figs.**
330 **3c,d**). However, larger-scale reorganization of the barotropic tidal energy fluxes under FRIS
331 also occurs (see, e.g., Rosier et al. (2014) and Padman et al. (in press)), so that simple
332 scaling of modern tidal currents by the change in *wct* is not possible.

333 **3.2 Spatial pattern of melt rates (w_b) in the base simulations**

334 We analyzed the six base simulations described in **Sect. 2.3.2** to quantify the sensitivity of
335 the spatial pattern of basal melt rates (w_b) to θ_{init}, tides, and geometry.

336 **3.2.1   Base simulation "no-tides" cases**

337 The pattern of w_b in the standard cold no-tides case (**Fig. 5a**) is generally consistent with the
338 increase in thermal forcing at the ice base $\left(\Delta T = \left(T_f - T_o \right) \right)$ due to the depression of the in
339 situ freezing point temperature of seawater (T_f) as pressure increases. The greatest values of
340 w_b occur along the deepest grounding lines (see **Fig. 2** for geometry), notably in the Support
341 Force, Foundation, and Rutford inlets. This pattern of pressure-dependent melt fuels the ice
342 pump mechanism that drives thermohaline circulation within the cavity and causes
343 refreezing conditions ($w_b < 0$) as melt water ascends to the mid-ice-shelf regions, as can be

14

344   seen under the central RIS and near the RIS ice front. Since our model does not include a

345   mechanism for frazil-ice formation, these regions represent where ice would form by direct

346   freezing onto the ice base.

347   The pattern of w_b for the standard warm no-tides case (**Fig. 5b**) is generally similar to the

348   standard cold no-tides case (**Fig. 5a**) but with an increase, by a factor of about 3.5, in the

349   shelf-averaged value. Changing cavity shape while imposing the same initial ocean

350   temperature in the modified warm case (**Fig. 5c**) only slightly reduces melt rates (by 10%)

351   for the no-tides scenario (compare **Figs. 5b and 5c**).

352   **3.2.2   Base simulation "tide-forced" cases**

353   Adding tide forcing to the standard cold case changes the magnitude and pattern of w_b

354   (compare **Figs. 5a and 5d**). Melt rates increase around the grounding line and in South

355   Channel, (**Fig. 5g**). The increase in w_b in South Channel, where tidal currents are relatively

356   strong, from the standard no-tides to tide-forced cases exceeds 2 m a^{-1}. Adding tides also

357   increases refreezing in portions of RIS, including north of Korff Ice Rise and along the coast

358   of the northwestern RIS, with more limited refreezing north of Henry Ice Rise. This increase

359   in refreezing with tides can be explained by the increased production of cold, buoyant

360   meltwater from the deeper parts of the ice shelf near the grounding line, and is qualitatively

361   consistent with the effects of adding tides reported by Makinson et al. (2011).

362   In the standard warm case, w_b also increases around the deep grounding lines when tides

363   are added (compare **Figs. 5b and 5e**). In this case, however, this increased melt doesn't

364   enhance mid-shelf basal freeze conditions as much as in the standard cold case.

365   Consequently, the increase of refreezing under the RIS is less pronounced than for the

366   standard cold tide-forced case (compare **Figs. 5e and Fig. 5d**). There are two possible

367   factors contributing to this result. First, the meltwater product at the deepest grounding lines

368   in the warm case is warmer than in the cold case and, hence, has a smaller potential for

15

369   supercooling when reaching shallower parts of the ice base. Second, the rising meltwater

370   may continue to warm on its ascent due to admixture of warmer ambient water in the ice

371   shelf cavity. Both factors are consistent with an increase in thermohaline circulation in

372   response to warmer ocean temperatures.

373   The modified warm tide-forced case (**Fig. 5f**) also exhibits a similar amplification of

374   basal melt by tides as the standard warm tide-forced case, although with regional differences

375   (compare **Figs. 5i and 5h**).

376   The differences between the tide-forced and no-tides cases for all three model setups

377   (**Fig. 5g-5i**) show that the principal effect of tides is to increase w_b under FIS and South

378   Channel.

379   **3.3 Sensitivity of w_b to tides, θ_{init} and geometry in the base simulations**

380   We summarize the effect of θ_{init} and geometry through values averaged over the ice shelf

381   area. Net mass change (M_b: Gt a^{-1}) and averaged values of w_b were calculated for three

382   regions: (*1*) all of FRIS, (*2*) areas for which melting conditions are predicted ($w_b > 0$), and

383   (*3*) areas where freezing conditions are predicted ($w_b < 0$). The ratio of M_b and w_b for the

384   freeze-only and melt-only calculations of mass change are not constant, since M_b is

385   influenced by the extent of melting and freezing regions as well as by the mean magnitude

386   of w_b.

387   Ocean temperature is the dominant control on total ice-shelf-integrated M_b and ice-shelf

388   averaged w_b (**Fig. 6**; **Table 2**). Regardless of tides and geometry, warming the ocean inflow

389   by 0.5^{o}C increases net mass loss by a factor of ~3-5. The integrated mass gain due to

390   freezing (marine ice formation) is insensitive to temperature for the no-tide cases but

391   sensitive to temperature for the tide-forced cases (**Fig. 6a**), suggesting that accurate

392   predictions of marine ice formation requires accurate representation of tidal currents in

393   simulations.

16

394　　　　Tides change the effect of ocean heat on distributions of M_b and w_b. In particular, the

395　　addition of tides to the standard cold case (our approximation to the modern state) increases

396　　net freezing by a factor of four, almost exactly offsetting a factor of ~2 increase in mass loss

397　　in melt-only regions. For the warm cases, tides increase total mass loss in melting regions by

398　　about 20–40%, with most of this increase occurring in South Channel and under FIS (see

399　　**Fig. 5**). In contrast to the cold case, the increases in net freezing in the warm cases is small

400　　compared with the increased mass loss, so that the total basal mass loss for FRIS increases

401　　significantly when tides are added to a warm ocean. ~~We attribute this result to production of~~

402　　~~a warmer plume near the deep grounding lines as a result of heat in the mixed layer that isn't~~

403　　~~fully utilized to fuel melting.~~

404　　　　　Changing geometry has a much smaller but still significant effect on ice-shelf-

405　　integrated M_b and averaged w_b. In the no-tides simulations, the change from standard to

406　　modified geometry causes net mass loss to increase slightly~~, suggesting a weak positive~~

407　　~~feedback,~~ while the tide-forced cases show a slight decrease~~, or negative feedback~~ (**Fig. 6**).

408　　This change in sign in the mass loss anomaly is driven primarily by the anomalous behavior

409　　of South Channel, and will be discussed in greater detail in **Sects. 3.4 and 4.2**.

3.4 Regional sensitivity of w_b in the base simulations

411　　Regional averages of w_b (**Fig. 7**) indicate that basal mass loss near the grounding lines of

412　　major inflowing ice streams varies by an order of magnitude within a given simulation.

413　　Support Force, Foundation, and Rutford ice streams show the largest values, exceeding 2 m

414　　a^{-1} for the standard cold cases with and without tide forcing. In contrast, modeled melt rates

415　　for Möller and Institute ice streams are in the range of 0.28–0.44 m a^{-1} for the standard cold

416　　case runs.

417　　　　　For each ice stream inlet, θ_{init} is the primary control on melt rate near the grounding line,

418　　with mean melt rate approximately doubling from the standard cold case to the standard

419 warm case. Tidal forcing is a secondary control that leads to either an increase or decrease in

420 w_b near grounding lines. For Support Force, Foundation, and Rutford ice streams, adding

421 tides reduces area-averaged melt rates, with the relative change being larger for the warm

422 cases with both standard and modified geometry. The largest fractional change in melt rate

423 due to tides occurs near the Rutford Ice Stream grounding line in the modified-geometry

424 warm case, where adding tides reduces mean melt rate by 40% from 7.7 m a^{-1} to 4.6 m a^{-1}.

425   South Channel is an exception to the general result that regional sensitivity of w_b is

426 more strongly affected by changes in θ_{init} than tidal forcing. In this region, w_b increases by

427 roughly an order of magnitude between the no-tide and tide-forced simulations, whereas the

428 fractional change due to θ_{init} is much smaller, about a factor of ~2 (**Fig. 7**). South Channel

429 also experiences a large reduction (~30%) in regionally-averaged w_b in the modified warm

430 tide-forced run compared with the standard warm tide-forced run. We attribute this change

431 in w_b to the reduction in tidal currents as geometry is changed (**Fig. 3**).

432 **3.5 Ocean circulation within the FRIS cavity in the passive-dye tracer simulations**

433 General patterns of water mass circulation into and under FRIS are demonstrated by output

434 from the two-year simulations with passive-tracer dyes (see **Sect. 2.3.3**). We focus only on

435 tide-forced simulations because, as discussed in **Sect. 3.3** and by Makinson et al. (2011),

436 tidal currents are known to be critical to patterns of basal melting beneath FRIS.

437 **3.5.1 Dye tracer circulation in standard cold tide-forced case**

438 The concentration of the open ocean bulk dye tracer in the upper σ-layer (**Fig 8a**) reveals

439 that the FRIS cavity has two different sources of heat inflow. The FIS and innermost RIS

440 cavities are flooded by a southward transport of the open continental shelf waters across the

441 FIS front, whereas the cavity circulation in the northeastern portion of RIS is dominated by

442 incursions of water from across the RIS front. The latter inflow does not penetrate deep into

18

the central and southern RIS within two years of simulation, although this is likely to be an artefact of the omission of the High Salinity Shelf Water that is known to be formed at the RIS front and is assumed to fuel gravity currents that reach the deep western grounding lines of the RIS. In our simulations, the water entering through FIS circulates clockwise along the deep grounding line. After two years, some dye has reached as far west as Carlson inlet; however, very little of this dye is found under the central RIS north of the ice rises and rumples. The most direct impact of changes in open ocean inflow is observed in Support Force and Foundation inlets, and in South Channel.

Meltwater produced near Foundation Ice Stream grounding line (**Fig. 8b**) reveals similar clockwise circulation. This water reaches the western RIS ice front in about two years. Meltwater from Foundation inlet flows into all ice stream inlets to the west of Foundation. The flow of this meltwater through South Channel is limited to the southern side of the channel.

Meltwater produced in South Channel also reaches all of the western RIS within two years (**Fig. 8c**), including much of the central region where refreezing occurs. Meltwater produced in Rutford inlet flows northward to the west of Korff Ice Rise (**Fig. 8d**).

These dye maps demonstrate that water found in the uppermost layer, in contact with the ice shelf base, in a specific ice stream inlet is a mixture of the incoming high-salinity ocean water and meltwater that was produced at other inlets further upstream. As an important consequence, changes in meltwater production in different regions will alter the meltwater plume characteristics (e.g., temperature) experienced by downstream ice stream grounding zones. In the following, it will be shown that the interactions within different grounding zone regions lead to non-local feedbacks of the melting response to changes in ocean temperatures and ice shelf geometry, for modeling of which an explicit inclusion of tidal currents is one of the key ingredients.

19

3.5.2 FRIS cavity dye tracer distribution for tide-forced cases

Comparisons of dye concentration maps after two years of integration for the three tide-forced simulations (**Fig. 9**) show differences that can be attributed both to θ_{init} (comparing standard cold and standard warm cases) and to geometry (comparing standard warm and modified warm cases).

The stronger cavity circulation introduced by the amplification of net basal melting for the warmer ocean, θ_{init} = -1.4°C, increases inflow through the FIS and into the RIS cavity (upper row of **Fig. 9**). Open-ocean water is present under most of RIS after two years in the standard warm case. The dye concentration of open-ocean water under the northern portion of RIS decreases as θ_{init} increases, indicating that the stronger northward flow of meltwater in the warm case reduces the contribution of the direct open-ocean inflow to the northern RIS. This influence of θ_{init} on strengthening the sub-ice-shelf cavity circulation decreases slightly in the modified warm case, which shows less open water dye penetrating into the innermost RIS than the standard warm case solution (compare the two upper right subplots of **Fig. 9**).

Comparisons of meltwater dyes from ice stream inlets and South Channel (lower six rows in **Fig. 9**) show, in all cases, more rapid ventilation of downstream regions when θ_{init} is warmer. In these simulations, meltwater dyes are injected continuously at a rate that is scaled to the basal melt rate (**Sect. 2.3.3**). Relative dye concentrations at specific locations can, therefore, be interpreted as the relative values of meltwater from different sources with total meltwater plume concentration being an integration of the contributions from all upstream sources. Changes in the different runs reflect the response of the cavity circulation and changes in meltwater production rate in the respective grounding zones. Meltwater from South Channel dominates the central RIS, although melting in Foundation and Rutford inlets provides a substantial freshwater flux to the western RIS.

20

493   The changes in upper-ocean circulation caused by changes in geometry, seen by
494   comparing the two warm cases in the last two columns of **Fig. 9**, are less obvious than the
495   effect of changing temperature. Nevertheless, changing geometry has a significant regional
496   effect. Foundation inlet meltwater spreads out more in the modified warm case than in the
497   standard warm case as a result of increased dye transport through the channel between
498   Henry Ice Rise and Berkner Island. South Channel meltwater concentrations are reduced in
499   the modified warm case, which is consistent with the reduced melt rates in the region
500   (**Fig. 5**). Similar to South Channel, Rutford inlet meltwater in the surface layer is also
501   reduced for the modified geometry case.

502   ### 3.5.3   Regional meltwater dye comparison, for tide-forced cases

503   Regional meltwater dye production and advection is evaluated from the surface levels of
504   Foundation, Möller, and South Channel inlet regions (as in **Fig. 4**). **Fig. 10** shows the
505   integrated values over these regions for the standard cold, standard warm and modified
506   warm tide-forced cases. As described in **Sect 2.3.3**, meltwater dye from a particular region is
507   a scaled quantity of w_b that reflects the magnitude of meltwater produced in that region. The
508   resulting passive dye is then transported through the domain through a combination of
509   advection and mixing and acts as a proxy for the meltwater plume. In this section, we use the
510   quantity of these meltwater tracers to demonstrate how meltwater circulation is affected by
511   changes in θ_{init} and geometry.

512   Foundation inlet shows an increase in integrated meltwater dye with the 0.5°C increase
513   in θ_{init} between the standard cold and standard warm cases (**Fig. 10a**). This increase in
514   integrated meltwater dye is not sustained with the change in cavity geometry. Instead, the
515   net amount of dye is reduced in the modified warm case such that the value of integrated dye
516   in the surface level more closely matches that of the standard cold case. This reduction in
517   integrated meltwater dye between the standard warm and modified warm case carries

21

518   forward into the Möller region, where the reduction of Foundation dye between the two
519   cases is even greater than in Foundation inlet (compare **Fig. 10a** and **10b**). At the same time,
520   the reduction in Foundation dye in the Möller region is somewhat compensated by the
521   Möller meltwater dye, which is consistent between the two warm cases (**Fig. 10b**). Overall,
522   the Möller region appears to be less affected by the change in geometry than the Foundation
523   region. Within South Channel, the influence of geometry on the quantity of meltwater dye is
524   compensated by changes in circulation that allow for more Foundation dye in the surface
525   level of South Channel in the modified warm case than the standard warm case (**Fig. 10c**).
526   This increase in surface level Foundation dye in South Channel is caused by changes in
527   circulation that distribute the dye more evenly across South Channel in the modified warm
528   case than in the standard warm case (**Fig. 9**).

529   These results highlight that the regional sensitivities of meltwater dye to θ_{init} and
530   geometry may influence but not necessarily determine the quantity and temperature of
531   meltwater in downstream regions. This result reveals the degree to which θ_{init} and cavity
532   shape precondition the quantity and origin of meltwater in any given region. For example,
533   the FRIS-integrated surface dye quantity (**Fig. 10e**) for Foundation and Support Force is
534   equivalent between the standard warm and modified warm cases, even though there are
535   strong regional variations in these cases (**Fig. 10 a-c**). In addition, the FRIS-integrated
536   values of meltwater dyes from the ice front regions (RIS west, RIS east, and FIS) are similar
537   among all cases while they differ among regions, showing greater amounts of dye in
538   Foundation, Möller, and South Channel regions for the warm cases than in the cold case.
539   These regional and integrated changes demonstrate that the FRIS meltwater product is a
540   result of regional feedbacks that are affected by a combination of production, mixing, and
541   advection.

4 Discussion

Our results confirm an earlier study (Makinson et al., 2011) demonstrating that adding tide forcing to numerical models substantially increases basal melting along the deep grounding lines of FRIS and increases marine ice formation rates under RIS. By carrying out simulations with different temperatures of water entering the sub-ice-shelf cavity, and investigating potential changes to ice draft in a scenario with a warmer ocean, we have also shown that the spatial patterns of melting and refreezing are sensitive to complex feedbacks between basal melting, tidal currents, advection and mixing.

The simplified forcing of our models, however, prevents the development of some sub-ice-shelf circulation features observed to be present in the modern state. The circulation under RIS is strongly affected by winter sea-ice formation and the associated production of High Salinity Shelf Water over the southern Weddell Sea continental shelf. Combined with larger-scale atmospheric forcing, these processes establish an east-to-west density gradient across the continental shelf (e.g. Foldvik et al., 1985; Nicholls et al., 2009) that drives a counter-clockwise circulation with inflow in the Ronne Depression and a counter-clockwise circulation around Berkner Is. (Foldvik et al. 2001). Our idealized model also lack the seasonal warming of the upper ocean near the ice front that leads to significant summer melting and rapid basal melting of the ice shelf frontal zone (e.g., Makinson and Nicholls, 1999; Joughin and Padman, 2003; Moholdt et al., 2014). Since we omit these forcings, our simulations do not capture these components of sub-ice-shelf circulation. As a result, our cold-case simulations are "present-day" in terms of ocean thermal forcing but with circulation that is more representative of the future-warming scenario presented by Hellmer et al. (2012). These simplifications restrict the predictive capacity of our simulations but help us clarify the importance of tidal currents and tide-related feedbacks that affect future mass loss from FRIS and the adjacent buttressed, grounded ice.

4.1 Comparison of modeled, ice shelf averaged basal melt estimates with observations

The melt rate averaged over the area of an ice shelf is a common metric for evaluating ice shelf mass balance (e.g., Rignot et al., 2013; Depoorter et al., 2013). Our estimate of melt rate averaged over FRIS for the standard case is 0.14 m a^{-1} freshwater equivalent, equal to ~48 Gt a^{-1} of net mass loss (**Fig. 6** and **Table 2**). The range of values reported by other studies extends from 0.03 m a^{-1}, the lower bound in Depoorter et al. (2013), to 0.55 m a^{-1} from the first oceanographically-derived estimates (Jenkins, 1991; Jacobs et al., 1992); see **Fig. 11** and **Table 3**. The range in estimates of w_b is a result of variations in observation type and model choices. Estimating w_b from observations typically requires averaging other ice shelf mass budget terms, derived from satellite observations and atmospheric models, over several years. Estimates from models are affected by model setup.

Compared with the three most recent satellite-constrained estimates, our value is near the central estimate of 0.12 m a^{-1} of Depoorter et al. (2013), and near the lower limit of the ranges reported by Rignot et al. (2013) and Moholdt et al. (2014). Given the model simplifications discussed above, we regard the general agreement between our integrated mass loss and prior studies as evidence that our simulations are sufficiently realistic for further sensitivity studies and interpretation of the role of tides in FRIS evolution for future climate states.

4.2 Sensitivity of w_b to ΔT and surface currents

We explore the regional variations of thermal forcing (ΔT) and turbulent exchange (u_*) on w_b using the 30-day averaged values from the end of each simulation to calculate ΔT and $|\mathbf{u}|$. Note that w_b in the 30-day averaged model output is based on the average of instantaneous heat fluxes and, therefore, includes the model's knowledge of covariances between ΔT and $|\mathbf{u}|$ on much shorter time scales. In contrast, $|\mathbf{u}|$ is calculated from 30-day averaged u- and v-

592   velocity components. We use a linear combination of non-tidal and tidal currents, U, given

593   by

594

595    $$\mathsf{U} = |\mathbf{u}|_{tide} + |\mathbf{u}| \quad [\text{m s}^{-1}], \tag{6}$$

596

597   where $|\mathbf{u}|_{tide}$ is from **Eq. (5),** to represent the local forcing for turbulent exchange. For the no-

598   tides cases, $|\mathbf{u}|_{tide}$ is zero and $\mathsf{U}_{\text{no tides}} = |\mathbf{u}|$. We include $|\mathbf{u}|_{tide}$ in the tide-forced cases to more

599   closely approximate the non-time-averaged relationship described by **Eq. (1),** because the

600   30-day average removes the tidal signal in ΔT and $|\mathbf{u}|$ in the tide-forced cases.

601   Comparisons of the six base simulations show that w_b generally follows the expected

602   functional dependence on ΔT and U (**Fig. 12a**): in all six cases, values of w_b increase with

603   stronger currents and more thermal forcing, with values roughly falling along lines of

604   constant $\Delta T \cdot \mathsf{U}$. In general, our values are in range of those shown in Holland et al. (2008),

605   (compare their Fig. 1 with our **Fig. 12b**), although regional differences can be seen in the

606   bivariate relationships between w_b and either ΔT or U (**Fig. 12b and 12c**). Most ice-stream

607   inlet averages show a similar increase in w_b with respect to ΔT (**Fig. 12b**), suggesting that

608   reasonable estimates of melt rate in the ice-stream inlets could be obtained from variability

609   of ΔT and a constant, assumed low, value of U. South Channel and, to some degree, Institute

610   inlet diverge from this relationship, demonstrating a larger variability in w_b in relation to ΔT

611   than is seen in other inlets (**Fig. 12b**). This larger variability in w_b in South Channel arises

612   because changes in modeled melt in this area are controlled primarily by changes in U (**Fig.**

613   **12b**).

614   Comparisons of the ratios for ΔT, U, and w_b at each site between simulations without

615   and with tides (**Fig. 12d-f**) show how each region responds to the combined effects of tide-

616   induced changes in ocean conditions. With the exception of South Channel, adding tides

617   always cools (decreases ΔT) the upper layer of ocean water adjacent to the ice base (**Fig.**

618   **12d**). On average, the largest reductions occur for the RIS ice stream inlets. We attribute this
619   result to cooling of water entering the RIS inlets by inclusion of meltwater from upstream
620   freshwater sources, with RIS inlets being influenced by rapid melting in Support Force and
621   Foundation inlets, and in South Channel (**Figs. 8 and 9**).

622   The differences between the tide-forced and no-tide cases show up more strongly in the
623   regionally-averaged comparison of $\cup$ (**Eq. (6), Fig. 12e**). In all regions, the effect of adding
624   tides is greater for the cold standard cases than for warm standard cases. Since the value of
625   $|\mathbf{u}|_{tide}$ in **Eq. (5)** is the same for the standard geometry runs, this difference represents the
626   increase in the thermohaline-driven $|\mathbf{u}|$ from the cold to warm cases.

627   The largest differences in $|\mathbf{u}|$ amongst all three model runs are in Möller, South Channel,
628   and Institute inlets. For the warm cases, modifying the geometry increases the ratio of $\cup_{tide\text{-}}$
629   $_{forced}$ / $\cup_{\text{no tides}}$ for these three regions even though tidal currents decrease (**Fig. 3**) as *wct*
630   increases. This response implies that $\cup_{\text{no tides}}$ also declines in the modified geometry case. A
631   decline in $\cup_{\text{no tides}}$ in the modified geometry is consistent with a reduction in z_{ice} in the inlet
632   regions, which would reduce the thermal forcing and, hence, reducing the ice pump
633   circulation. If true, this feedback is an artefact of our model geometry, which excludes the
634   possibility of deeper ice that could be exposed when the grounding line migrates due to the
635   imposed thinning. Corollary evidence for this reduction in ice pump circulation is seen in the
636   top row of **Fig. 9**.

637   The role of South Channel melt on cooling downstream ice stream inlets, its sensitivity
638   to tides, and tidal sensitivity to changing z_{ice} suggest that reliable predictions of change in
639   modeled w_b in the southern RIS ice streams for future climate scenarios depends on the
640   correct representation of changes to South Channel geometry.

4.3 Role of advection through South Channel

As the maps of surface-layer dye tracers (**Fig. 8 and 9**) show, most water entering the FRIS cavity in our simulations flows southward under the FIS front and then circulates clockwise around the FIS and RIS grounding lines. A water parcel takes about two years to travel from the FIS front to the southwestern RIS region of Rutford inlet. During that time, each water parcel is subjected to mixing with meltwater, so that the properties of water entering each inlet depend on the processes along the entire upstream path. Meltwater produced along each flow path continues to circulate clockwise with the inflowing warmer and saltier water that originated north of the ice front; see, e.g., dye distribution representing meltwater from Foundation inlet (**Fig. 8b**).

Water near the ice base in South Channel contains significant freshwater contributions from Support Force and Foundation inlets, with a smaller contribution from Möller inlet (Fig. 9). ~~Since~~ circulation ~~in our simulations~~ is driven only by thermohaline circulation ~~modified by tides~~, these pathways. ~~Our model excludes the influences of wind-driven circulation and sea-ice formation~~,,so these dye distributions are qualitatively similar to those ~~shown by Holland et al. (2007)~~. A north-south transect across the western end of South Channel (**Fig. 13**), shows that all water within that transect is colder (and fresher; not shown) than θ_{init}; i.e., some meltwater from upstream is present at all depths, with the path-integrated volume of added meltwater setting the buoyancy that drives stratification. Further, distributions of meltwater contributions from individual regional sources also vary in the vertical (**Fig. 13**). The standard geometry simulations show a core of open water dye along the bottom and northeastern slope of the trough under South Channel. Support Force dye is concentrated near the ice base, toward the southwestern end of the transect. Foundation dye appears in both the surface and deep model layers, concentrated on the southern side of South Channel (see, also, **Fig. 8b**). The bifurcation of Foundation dye in South Channel reflects two sources; one in which fairly pure inflow water melts ice in Foundation inlet and

27

then flows directly into deeper portions of South Channel, and one stream that then experiences further cooling and freshening near the ice base from interactions with the ice in Möller inlet and South Channel to the east of the transect. As expected, South Channel dye has the highest concentration in the surface waters of this transect.

The spatial pattern in dye distribution is fairly consistent between the warm and cold standard geometry cases, although much more open water dye from north of the ice front is present in the warm case. This quantitative difference is consistent with the overall understanding that warmer θ_{init} drives a stronger thermohaline circulation that enhances cavity circulation and leads to a shorter residence time (**Fig. 9**).

More qualitative differences between simulations arise from the change in cavity shape. Except for South Channel dye, the modified geometry shows more laterally uniform dye concentrations across the channel. Dye distribution remains vertically stratified in all three cases with the depth of the upper layer being similar in the standard warm and modified warm cases. However, even though the averaged w_b in South Channel is similar between the standard cold and modified warm cases (**Fig. 7**), the South Channel meltwater product does not mix down as far in the modified warm case as it does in the standard cold case (**Fig. 13**), which we attribute to the much weaker tidal currents in this region (**Fig. 3**) for modified geometry.

Transects for dye tracers are only provided for the tide-forced cases. However, a comparison of temperature transects for the no-tides and tide-forced cases (**Fig. 13**) show that the thermocline is deeper in the standard geometry tide-forced cases, with the thermocline most affected in the standard cold case. As shown in **Fig. 12d**, tides increase the thermal forcing in South Channel in the standard geometry by a factor of ~3 while having a negligible effect on ΔT in the modified geometry. These results suggest that the lowered thermocline in this region is caused by tide-induced mixing rather than advection, so that its depth responds to the reduced tidal currents in the modified warm case.

28

4.4 Implications of regional melt on ice sheet mass balance

Walker et al. (2008) showed that the spatial distribution of ice shelf melt rates was critical to the behavior of the buttressed grounded-ice streams; for the same integrated mass loss from an ice shelf, grounded-ice loss was significantly faster when the melting was concentrated near the grounding line. Gagliardini et al. (2010) confirmed this analysis and also noted that a grounded-ice stream could thicken, and its grounding line could advance even when net melting increased, if the melt rate decreased near the grounding line. In the context of our study the implication is that, even when the change in the ice-shelf area-averaged melt rate is small, substantial variability in melt rates near ice-stream grounding lines could still have a large impact on loss (or gain) of grounded ice.

In addition to being affected by the spatial distribution of w_b, dynamic mass loss of grounded ice is also affected by bedrock slope and ice sheet topography. These factors introduce additional spatial heterogeneity in the influence of basal melting on overall mass loss from the grounded ice streams flowing into FRIS. Wright et al. (2014) used the BISICLES ice sheet model to test the sensitivity of the grounded ice sheet to changes in FRIS mass loss at the grounding line. They found that Institute and Möller ice streams are the most sensitive to changes in basal mass balance that might be caused by a warming ocean inflow. This result was confirmed by Martin et al. (2015) using the Parallel Ice Sheet Model (PISM). These two ice streams rest on top of steep reverse bed slopes with low basal roughness, conditions which have been shown to contribute to grounding line instability and retreat (Schoof, 2007). Furthermore, these ice streams are also sensitive to changes in the buttressing effect from ice shelf mass change around Henry and Korff ice rises and the associated change in basal sliding over these ice rises. Our results indicate that tides currently exert a strong influence on basal mass balance in the area around Henry and Korff ice rises (**Fig. 5**), by increasing melting in South Channel and increasing marine ice accretion north of the ice rises and Doake Ice Rumples.

29

719   Möller and Institute are among the lowest meltwater producing regions (**Fig. 7**) and

720   receive the largest fraction of meltwater product from Foundation inlet basal melt (**Fig. 10**).

721   The relative quantities of these meltwater products are sensitive to changes in advection and

722   mixing imposed by changes in θ_{init} and geometry (**Sec. 3.5**). As shown in **Fig. 7**, the 0.5°C

723   increase in θ_{init} increases the Möller grounding-line region w_b to 1.03 m a^{-1} (an increase of

724   134%) and Institute grounding-line region w_b to 1.30 m a^{-1} (an increase of 100%), for the

725   tide-forced cases. The grounding lines in these regions appear to be very sensitive to changes

726   in θ_{init} and less sensitive to changes in the cavity ocean circulation imposed by a change in

727   model geometry. Even with Möller and Institute's sensitivity to θ_{init}, however, these inlets

728   are buffered from variations in open ocean heat due to the combined influence of circulation

729   pathways and inflowing meltwater derivatives (**Fig. 10**).

730   Of the nine grounding-line regions explored in this study, Foundation inlet has the

731   highest averaged melt rate of 2.76 m a^{-1} for the standard cold case (**Fig. 7**), a rate which

732   more than doubles to 6.01 m a^{-1} when θ_{init} increases from -1.9°C to -1.4°C. However,

733   grounded-ice mass flux from Foundation Ice Stream is less sensitive to changes in basal

734   melting than Möller and Institute (Wright et al., 2014). According to the results presented in

735   Wright et al. (2014), even the higher melt rate with the warmed ocean in our study is

736   insufficient to drive grounding line retreat and significant acceleration of grounded-ice loss

737   through Foundation inlet. Therefore, it is possible that the dominant effect on the grounded-

738   ice mass budget of large w_b at Foundation is through the effect of Foundation inlet meltwater

739   on downstream inlets, particularly Möller. As shown in the dye results presented in **Sect.**

740   **3.5**, Möller is somewhat isolated from FIS inflow but flooded by Foundation meltwater.

741   **4.5 Implications of regional freeze conditions on ice sheet mass balance**

742   As described in **Sect. 3.2.1** and **Sect. 3.2.2**, refreezing occurs in our simulations throughout a

743   large region of the central RIS. Refreezing in this region is qualitatively consistent with

30

estimates of basal mass balance from satellite-based remote sensing (e.g., Joughin and Padman, 2003; Rignot et al., 2013; Moholdt et al., 2014). The extent of freezing conditions is important because marine ice accretion supports ice shelf stability through its effect on the mechanical properties of ice (Kulessa et al., 2014; McGrath et al., 2014; Li et al., submitted) and by altering the extent of grounding on topographic highs such as ice rises and rumples.

Our standard cold tide-forced case produces local maxima in marine ice growth rates in the northwestern RIS, the region northeast and east of Korff Ice Rise, and the region to the north and west of Henry Ice Rise (**Fig. 5d**). These regions of freezing are broadly consistent in all our model runs (**Fig. 5**) and the net mass increase in refreezing regions are increased when tide forcing is added (**Fig. 6**). Our standard cold tide-forced case has roughly four times more mass gain than the standard cold no-tides case, generally consistent with Makinson et al. (2011). In both warm cases, standard and modified geometry, adding tides increases net marine ice formation by a factor of two. That is, tides will continue to be important for marine ice accretion beneath FRIS if ocean temperatures rise as predicted by Hellmer et al. (2012, 2017) and will, therefore, continue to play a role in FRIS ice shelf stability.

5 Conclusions

The idealized modeling results presented here on the basal melting of FRIS, combined with ice-sheet model results reported by Wright et al. (2014), indicate that the response of the Antarctic Ice Sheet in the Weddell Sea sector to large-scale ocean circulation changes depends on several regional and local processes that combine to determine ocean state in individual ice-stream inlets. These processes include the tidal contribution to ocean mixing, advection of meltwater products into downstream inlets, and feedbacks between advection, tides and melting as ice shelf draft evolves.

768   In general, tides increase the area-integrated mass loss from the entire FRIS, consistent

769   with the findings of Makinson et al. (2011); however, for our cold case ocean representing

770   the modern state, increased basal melting with tides is completely offset by a factor-of-four

771   increase in freezing (marine ice formation) in the central Ronne Ice Shelf.

772   As proposed by Hellmer et al. (2012), warming of water entering the cavity under FRIS,

773   primarily as an inflow under the FIS front, leads to a large increase in ice-shelf-integrated

774   mass loss. In our simulations, warming of 0.5°C increased total FRIS mass loss by a factor

775   of ~3.6 for the no-tides simulations (cf. Hellmer et al., 2012) and by a factor of ~5.1 when

776   tidal forcing was included.

777   The large-scale sub-ice-shelf circulation in our idealized model is dominated by a

778   southward inflow of open-ocean water across the Filchner Ice Shelf front, and clockwise

779   circulation of this water along the southern grounding line. This clockwise sub-ice-shelf

780   circulation is, in part, a consequence of our simplified model forcing, which excludes some

781   inflows that would be forced by realistic spatial and seasonal variability in the open ocean

782   north of the ice shelf. Under this circulation regime, a water parcel takes about two years to

783   travel from the Filchner ice front to the southwestern Ronne Ice Shelf.

784   At the regional scale, complex feedbacks occur between local processes such as tide-

785   induced mixing and advection, so that the temperature of a water parcel represents the

786   upstream integrated history of mixing between the inflowing source water and basal

787   meltwater. The temperature of the upper ocean layer adjacent to the ice shelf base is cooler

788   when tide forcing is included, especially in the southwestern Ronne ice stream inlets

789   (Rutford, Carlson and Evans). We attribute this cooling to incorporation of meltwater from

790   upstream sources, notably Foundation inlet and South Channel.

791   Our results show regionally variable responses to changes in tides, θ_{init}, and cavity

792   geometry that can be summarized as follows.

793   (1)   Meltwater plumes from basal melting introduce non-local feedbacks, within the

794   same cavity, in response to variations of inflowing ocean heat and melt-induced

795   changes in ice draft.

796   (2)   Adding tide forcing to models increases w_b under the FIS and portions of the

797   RIS, with the largest increase within South Channel.

798   (3)   Adding tide forcing increases integrated marine ice formation for all three cases

799   including the two warm cases. The tidal contribution to ice-shelf dynamics will

800   persist through future ocean warming of at least 0.5^{o}C and may increase ice

801   sheet grounding and associated contact stresses in the region near Henry and

802   Korff ice rises and Doake Ice Rumples.

803   (4)   In some regions (e.g. South Channel), tides influence w_b directly by changing

804   the friction velocity; in other regions (e.g., Rutford), tides influence meltwater

805   production through changes in θ by mixing along the upstream flow path. ~~Tides~~

806   ~~affect how w_b changes in response to θ_{mit} and cavity geometry by these direct~~

807   ~~and indirect influences.~~

808   (5)   The greatest fraction of meltwater in the Möller and Institute inlets are

809   contributed by basal melting in Foundation inlet, indicating that increased

810   meltwater production in one inlet may reduce melting in a downstream inlet.

811   The regional distributions of meltwater and w_b are sensitive to the accuracy of our grids

812 of seabed depth and *wct*, which are based on few passive seismic measurements in regions

813 of strong model sensitivity (**Fig. 3f**). Distributions are also affected by the model

814 configuration, including neglect of atmospheric and sea-ice forcing, the choice of mixing

815 schemes and the thermodynamic exchange coefficients for the ice-ocean boundary layer

816 parameterization. Nevertheless, our analysis shows that the interplay of tides, far-field

817 thermal forcing and the oceanic response to ice shelf geometry changes leads to complex

818 and sometimes non-local interactions that alter the overall basal mass balance that effects
819 melting near the grounding lines, thereby controlling the dynamical response of adjacent
820 grounded ice streams.

821 Estimates of the future mass loss through the ice streams draining the West Antarctic
822 Ice Sheet into Ronne Ice Shelf, in climate scenarios where the heat flux into the cavity under
823 FRIS increases, are sensitive to how the ice draft in South Channel evolves. Under modern
824 conditions and with the seabed and ice draft represented by the RTOPO-1 database, tides are
825 a critical contributor to basal melting in that region. A warmer ocean will increase mass loss
826 by basal melting that will lead to ice shelf thinning unless it is offset by increased inputs
827 from ice advection and snowfall. However, this thinning then causes regional feedbacks that
828 include a reduction in basal melting in South Channel, as tidal currents weaken, a change in
829 circulation pathways with consequences for heat and meltwater transport and, possibly, a
830 dynamic response of the grounded ice that may offset ocean-driven thinning of the ice shelf.
831 We conclude that it is not possible to predict the true effect of oceanic warming on ice
832 thinning near individual ice stream grounding lines without a better understanding of the
833 feedbacks introduced by tidal forcing and circulation as a result of changes in *wct*. That is, as
834 coupled ocean/ice-sheet models become a standard tool for projecting ice sheet response to
835 changing climate, tides must be either explicitly modeled, or represented by a
836 parameterization that itself can evolve with time at a rate set by the evolution of the cavity.
837 Furthermore, potential bottlenecks in sub-ice-shelf circulation of ocean heat must be
838 identified through improved surveys of seabed bathymetry which, when combined with the
839 better-known ice shelf draft, determines both the tidal current speeds and the mean ocean
840 circulation towards downstream sites including ice-stream inlets. While FRIS is presently in
841 approximate steady state, the potential for future ocean warming, increased w_b, and a
842 corresponding mass loss causing a ~1 m sea-level rise supports the need to augment

34

843   measurements of the seabed bathymetry beneath FRIS, particularly within the ice stream

844   inlet regions and under South Channel.

Author contribution

846   R.D.M. led the study. The simulations were designed by R.D.M. and L.P., implemented by

847   R.D.M. and S.L.H., and analyzed by R.D.M., L.P. and T.H. The paper was written

848   by R.D.M., L.P. and T.H.

Acknowledgements

References

859   Arzeno, I. B., Beardsley, R. C., Limeburner, R., Owens, B., Padman, L., Springer, S. R.,

860   Stewart, C. L., and Williams, M. J. M.: Ocean variability contributing to basal melt rate

861   near the ice front of Ross Ice Shelf, Antarctica, J. Geophys. Res. Oceans, 119, 4214–

862   4233, doi:10.1002/2014JC009792, 2014.

863   Beckmann, A. and Haidvogel, D.B.: Numerical simulation of flow around a tall isolated

864   seamount. Part 1: Problem formulation and model accuracy, J. Phys. Oceanogr., 23,

865   1736–1753, 1993.

866   Chapman, D.: Numerical treatment of cross-shelf open boundaries in a barotropic coastal

867   ocean model, J. Phys. Oceanogr., 19, 384–391, 1985.

868   Christianson, K., Bushuk, M., Dutrieux, P., Parizek, B.R., Joughin, I.R., Alley, R.B., Shean,

869   D.E., Abrahamsen, E.P., Anandakrishnan, S., Heywood, K.J., Kim, T.W.: Sensitivity of

870   Pine Island Glacier to observed ocean forcing. Geophys. Res. Lett. **43**, 10817–10825,

871   doi: 10.1002/2016GL070500, 2016.

872   Darelius, E., Fer, I., and Nicholls, K. W.: Observed vulnerability of Filchner-Ronne Ice

873   Shelf to wind-driven inflow of warm deep water. Nature Comms., 7, 2016.

874   Depoorter, M., Bamber, J. , Griggs, J. , Lenaerts, J. , Ligtenberg, S. , van den Broeke, M.,

875   and Moholdt, G.: Calving fluxes and basal melt rates of Antarctic ice shelves, Nature,

876   502, 89–92, doi:doi:10.1038/nature12567, 2013.

877   Dinniman, M. S., Klinck, J. M., and Smith Jr., W. O.: Influence of sea ice cover and icebergs

878   on circulation and water mass formation in a numerical circulation model of the Ross

879   Sea, Antarctica. J. Geophys. Res., 112, C11013, doi:10.1029/2006JC004036, 2007.

880   Dinniman, M. S., Klinck, J. M. , and Smith, Jr., W. O.: A model study of Circumpolar Deep

881   Water on the West Antarctic Peninsula and Ross Sea continental shelves, Deep-Sea Res.

882   II., 58, 1508–1523, doi:10.1016/j.dsr2.2010.11.013, 2011.Dupont, T. K. and Alley, R.

883   B.: Assessment of the importance of ice-shelf buttressing to ice-sheet flow. Geophys.

884   Res. Lett. 32, L04503, 2005.

885   Flather, R.: A tidal model of the northwest European continental shelf, Memoires de la

886   Societé Royale des Sciences de Liége, 6, 141–164, 1976.

887   Foldvik, A., and Kvinge, T.: Conditional instability of sea water at the freezing point, Deep

888   Sea Res., 21, 169–174, 1974.

Foldvik, A., Gammelsrød, T., and Tørresen, T.: Circulation and water masses on the Southern Weddell Sea Shelf, in Oceanology of the Antarctic Continental Shelf, Antarct. Res. Ser., vol. 43, edited by S. S. Jacobs, pp. 5–20, AGU, Washington, D. C., 1985.

Foldvik, A., Gammelsrød, T., Nygaard, E. and Østerhus, S.: Current meter measurements near Ronne Ice Shelf, Weddell Sea: Implications for circulation and melting underneath the Filchner-Ronne ice shelves, J. Geophys. Res., 106 (C3), 4463–4477, 2001.

Gagliardini, O., Durand, G., Zwinger, T., Hindmarsh, R. C. A. and Le Meur, E.: Coupling of ice shelf melting and buttressing is a key process in ice-sheet dynamics, Geophys. Res. Lett., 37, L14501, doi:10.1029/2010GL043334, 2010.

Gammelsrød, T., et al.: Distribution of water masses on the continental shelf in the southern Weddell Sea, in Polar oceans and their role in shaping the global environment, edited by M. Johannessen, R. D. Muench, and J. E. Overland, pp. 159–175, American Geophysical Union, Washington, D. C., 1994.

Gerdes, R., Determann, J., and Grosfeld, K.: Ocean circulation beneath Filchner-Ronne Ice Shelf from three-dimensional model results, J. Geophys. Res., 104 (C7), 15,827–15,842, 1999.

Groh, A., and Horwath, M.: The method of tailored sensitivity kernels for GRACE mass change estimates. Geophys. Res. Abstr., 18, EGU2016-12065, 2016.

Haney, R. L.: On the pressure-gradient force over steep topography in sigma coordinate ocean models, J. Phys. Oceanogr., 21(4) 610–619, 1991.

Harig, C., and Simons, F. J.: Accelerated West Antarctic ice mass loss continues to outpace East Antarctic gains, Earth Planet. Sci. Lett., 415, 134–141, 2015.

Hellmer, H. H., and Olbers, D. J.: A two-dimensional model for the thermohaline circulation under an ice shelf, Antarct. Sci., 1 (4), 325–336, 1989.

913 Hellmer, H. H.: Impact of antarctic ice shelf basal melting on sea ice and deep ocean
914   properties, Geophys. Res. Lett., 31 (10), L10307, doi:0094-8276/04/2004GL019506,
915   2004.

916 Hellmer, H. H., Kauker, F., Timmermann, R., and Hattermann, T.: The fate of the southern
917   Weddell Sea continental shelf in a warming climate, J. Climate, 2017.

918 Hellmer, H. H., Kauker, F., Timmermann, R., Determann, J., and Rae, J.: Twentyfirst-
919   century warming of a large Antarctic ice-shelf cavity by a redirected coastal current,
920   Nature, 485, 225–228, doi:10.1038/nature11064, 2012.

921 Holland, D. M., and Jenkins, A.: Modeling thermodynamic ice-ocean interactions at the base
922   of an ice shelf, J. Phys. Oceanogr., 29 (8), 1787–1800, 1999.

923 Holland, P. R., Feltham, D.L., Jenkins, A.: Ice Shelf Water plume flow beneath Filchner-
924   Ronne Ice Shelf, Antarctica, J. Geophys. Res., 112, C05044,
925   doi:10.1029/2006JC003915, 2007.

926 Holland, P.R., Jenkins, A., Holland, D.M.: The Response of Ice Shelf Basal Melting to
927   Variations in Ocean Temperature. J. Climate, 21, 2558–2572,
928   https://doi.org/10.1175/2007JCLI1909.1, 2008.

929 Jacobs, S. S., Hellmer, H. H., Doake, C. S. M., Jenkins, A. and Frolich, R. M.: Melting of
930   ice shelves and the mass balance of Antarctica, J. Glaciol., 38(130), 375–387, 1992.

931 Jacobs, S., Giulivi, C., Dutrieux, P., Rignot, E., Nitsche, F. and Mouginot, J.: Getz Ice Shelf
932   melting response to changes in ocean forcing. Journal of Geophysical Research: Oceans,
933   118(9), pp.4152-4168, 2013.

934 Jenkins, A.: A one-dimensional model of ice shelf-ocean interaction, J. Geophys. Res.-
935   Ocean., 96(C11), 20,671–20,677, 1991.

936 Jenkins, A., Hellmer, H.H., and Holland, D.M.: The role of meltwater advection in the
937   formulation of conservative boundary conditions at an ice-ocean interface, J. Phys.
938   Oceanogr., 31, 285–296, 2001.

939   Jenkins, A., Nicholls, K. W., and Corr, H. F. J.: Observations and parameterization of
940   ablation at the base of Ronne Ice Shelf, Antarctica, J. Phys. Oceanogr., 40, 2298–2312,
941   2010a.

942   Jenkins, A., Dutrieux, P., Jacobs, S.S., McPhail, S.D., Perrett, J.R., Webb, A.T., White, D.:
943   Observations beneath Pine Island Glacier in West Antarctica and implications for its
944   retreat. Nat. Geo., 3, 468–472, doi:10.1038/ngeo890, 2010b.

945   Joughin, I. and Padman, L.: Melting and freezing beneath Filchner-Ronne Ice Shelf,
946   Antarctica, Geophys. Res. Lett., 30 (9), 1477, doi:10.1029/2003GL016941, 2003.

947   Joughin, I., Smith, B. E., and Medley, B.: Marine ice sheet collapse potentially under way
948   for the Thwaites Glacier basin, West Antarctica, Science, 344, 735–738, 2014.

949   Khazendar, A., Rignot, E., Schroeder, D.M., Seroussi, H., Schodlok, M.P., Scheuchl, B.,
950   Mouginot, J., Sutterley, T.C. and Velicogna, I.: Rapid submarine ice melting in the
951   grounding zones of ice shelves in West Antarctica. Nat. Commun., 7, 2016.

952   Kobs, S., Holland, D. M., Zagorodnov, V., Stern, A. and Tyler, S. W.: Novel monitoring of
953   Antarctic ice shelf basal melting using a fiber‐optic distributed temperature sensing
954   mooring. Geophys. Res. Lett., 41(19), 6779–6786, 2014.

955   Kulessa, B., Jansen, D., Luckman, A.J., King, E., Sammonds, P.R.: Marine ice regulates the
956   future stability of a large Antarctic ice shelf. Nat. Commun. 5:3707 doi:
957   10.1038/ncomms4707, 2014.

958   Li, R., Xiao, H., Liu, S., and Tong, X.: A Systematic Study of the Fracturing of Ronne -
959   Filchner Ice Shelf, Antarctica, Using Multisource Satellite Data from 2001 to 2016, The
960   Cryosphere Discuss., https://doi.org/10.5194/tc-2017-178, in review, 2017.

961   MacAyeal, D.R: Thermohaline circulation below the Ross Ice Shelf: A consequence of
962   tidally induced vertical mixing and basal melting, J. Geophys. Res., 89(C1), 597–606,
963   1984.

964 Makinson, K., and K. Nicholls: Modeling Tidal currents beneath Filchner-Ronne Ice Shelf

965   and on the adjacent continental shelf: Their effect on mixing and transport, J. Geophys.

966   Res., 104(C6), 13,449–13,465, 1999.

967 Makinson, K., Schröder, M., and Østerhus, S.: Effect of critical latitude and seasonal

968   straticiation on tidal current profiles along Ronne Ice Front, Antarctica, J. Geophys. Res.-

969   Ocean., 111(C3), C03022, doi:10.1029/2005JC003062, 2006.

970 Makinson, K., Holland, P., Jenkins, A., Nicholls, K. W., and Holland, D. M.: Influence of

971   tides on melting and freezing beneath Filchner-Ronne Ice Shelf, Antarctica, Geophys.

972   Res. Lett., 38, L06601, doi:10.1029/2010GL046462, 2011.

973 Marchesiello, P., McWilliams, J. C., Shchepetkin, A.: Open boundary conditions for long-

974   term integration of regional oceanic models, Ocean Modeling, 3(1–2), 1–20, 2001.

975 Martin, M. A., Levermann, A., and Winkelmann, R.: Comparing ice discharge through West

976   Antarctic Gateways: Weddell vs. Amundsen Sea warming, Cryosphere Discuss., 9,

977   1705–1733, 2015.

978 McGrath, D., Steffen, K., Holland, P. R., Scambos, T., Rajaram, H., Abdalati, W., and

979   Rignot, E.: The structure and effect of suture zones in the Larsen C Ice Shelf, Antarctica,

980   J. Geophys. Res. Earth Surf., 119, 588–602, doi:10.1002/2013JF002935, 2014.

981 McPhee, M. G., Morison, J. H., and Nilsen, F.: Revisiting heat and salt exchange at the ice-

982   ocean interface: Ocean flux and modeling considerations, J. Geophys. Res.-Ocean., 113,

983   C06014, doi:10.1029/2007JC004383, 2008.

984 Mengel, M., Feldmann, J., Levermann, A.: Linear sea-level response to abrupt ocean

985   warming of major West Antarctic ice basin, Nat. Clim. Change, 6, 71–74,

986   doi:10.1038/nclimate2808, 2016.

987 Mercer, J.H.: West Antarctic ice sheet and CO_2 greenhouse effect: a threat of disaster,

988   Nature, 271, 321–325, 1978.

989 Moholdt, G., Padman, L., and Fricker, A.: Basal mass budget of Ross and Filchner-Ronne

990   ice shelves, Antarctica, derived from Lagrangian analysis of ICESat altimetry. J.

991   Geophys. Res.-Earth Surf., 119(11), 2361–2380, 2014.

992 Monaghan, A. J., Bromwich, D. H., Fogt, R. L., Wang, S. H., Mayewski, P. A., Dixon, D.

993   A., Ekaykin, A., Frezzotti, M., Goodwin, I., Isaksson, E. and Kaspari, S. D.: Insignificant

994   change in Antarctic snowfall since the International Geophysical Year, Science,

995   313(5788), 827–831, 2006.

996 Mouginot, J., Rignot, E., and Scheuchl, B.: Sustained increase in ice discharge from the

997   Amundsen Sea Embayment, West Antarctica, from 1973 to 2013, Geophys. Res. Lett.,

998   41, doi:10.1002/2013GL059069, 2014.

999 Mueller, R. D., Padman, L., Dinniman, M. S., Erofeeva, S. Y., Fricker, H. A., and King, M.

1000   A.: Impact of tide-topography interactions on basal melting of Larsen C Ice Shelf,

1001   Antarctica, J. Geophys. Res., 117, C05005, doi:10.1029/2011JC007263, 2012.

1002 Mueller, R.D.: The effects of thermodynamic parameterizations, ice shelf geometry, and

1003   tides on modeled basal melting of Weddell Sea ice shelves, doctoral dissertation, Oregon

1004   State University, http://ir.library.oregonstate.edu/xmlui/handle/1957/49292, 2014.

1005 Nicholls, K. W., Østerhus, S., Makinson, K., and Johnson, M. R.: Oceanographic conditions

1006   south of Berkner Island, beneath Filchner-Ronne Ice Shelf, Antarctica, J. Geophys. Res.-

1007   Ocean., 106 (C6), 11,481–11,492, 2001.

1008 Nicholls, K. W., Padman, L., Schröder, M., Woodgate, R. A., Jenkins, A., and Østerhus, S.:

1009   Water Mass Modification Over the Continental Shelf North of Ronne Ice Shelf,

1010   Antarctica, J. Geophys. Res.-Ocean., 108 (C8), 3260, 2003.

1011 Nicholls, K. W., and Østerhus, S.: Interannual variability and ventilation timescales in the

1012   ocean cavity beneath Filchner-Ronne Ice Shelf, Antarctica, J. Geophys. Res., 109,

1013   C04014, doi:10.1029/2003JC002149, 2004.

Nicholls, K. W., Østerhus, S., Makinson, K., and Gammelsrød, T., and Fahrbach, E.: Ice-ocean processes over the continental shelf of the southern Weddell Sea, Antarctica: A review, Rev. Geophys., 47, RG3003, doi:8755-1209/09/2007RG000250, 2009.

Padman, L., Fricker, H. A., Coleman, R., Howard, S., and Erofeeva, S.: A new tidal model for the Antarctic ice shelves and seas, J. Glaciol., 34, 247–254, 2002.

Padman, L., Siegfried, M. R., and Fricker, H. A.: The role of ocean tides on Antarctic and Greenland ice-sheet processes, Rev. Geophys, in press.

Paolo, F. S., Fricker, H. A. and Padman, L.: Volume loss from Antarctic ice shelves is accelerating, Science 348, 327–331, 2015.

Paolo, F. S., Fricker, H. A., & Padman, L.: Constructing improved decadal records of Antarctic ice shelf height change from multiple satellite radar altimeters. Remote Sens. Environ., *177*, 192–205, 2016.

Pritchard, H. D., Ligtenberg, S. R. M., Fricker, H. A., Vaughan, D. G., van den Broeke, M. R., and Padman, L.: Antarctic ice-sheet loss driven by basal melting of ice shelves, Nature, 484, 502–505, doi: 10.1038/nature10968, 2012.

Raymond, W. H. and H. L. Kuo: A radiation boundary condition for multi-dimensional flows, Quart. J. R. Met. Soc., **110**, 535-551, 1984.

Rignot, E., and Jacobs, S. S.: Rapid bottom melting widespread near Antarctic Ice Sheet grounding lines, Science, 296 (5575), 2020–2023, doi:10.1126/science.1070942, 2002.

Rignot, E., Mouginot, J., and Scheuchl, B.: Ice-shelf melting around Antarctica, Science, 341(6143), 266–270, doi:10.1126/science.1235798, 2013.

Rignot, E., Mouginot, J., Morlighem, M., Seroussi, H. and Scheuchl, B.: Widespread, rapid grounding line retreat of Pine Island, Thwaites, Smith, and Kohler glaciers, West Antarctica, from 1992 to 2011. Geophys. Res. Lett. 41, 3502–3509, 2014.

1038 Robertson, R., Padman, L., and Egbert, G.: Tides in the Weddell Sea, in Oceanology of the

1039   Antarctic Continental Shelf, Antarct. Res. Ser., vol. 75, edited by S. Jacobs and R.

1040   Weiss, pp. 341–369, AGU, Washington, D. C., 1998.

1041 Rosier, S. H. R., Green, J. A. M., Scourse, J. D., and Winkelmann, R.: Modeling Antarctic

1042   tides in response to ice shelf thinning and retreat, J. Geophys. Res. Oceans, 119(1), 87-

1043   97, 2014.

1044 Ross, N., Bingham, R. G., Corr, H. F., Ferraccioli, F., Jordan, T. A., Le Brocq, A., Rippin,

1045   D. M., Young, D., Blankenship, D. D., and Siegert, M.J.: Steep reverse bed slope at the

1046   grounding line of the Weddell Sea sector in West Antarctica, Nat. Geo., *5*(6), 393–396,

1047   2012.

1048 Scambos, T. A., Bohlander, J. A., Shuman, C. A., and Skvarca, P.: Glacier acceleration and

1049   thinning after ice shelf collapse in the Larsen B embayment, Antarctica, Geophys. Res.

1050   Lett., 31, L18402, doi:10.1029/2004GL020670, 2004.

1051 Schlosser, P., Bayer, R., Foldvik, A., Gammelsrød, T., Rohardt, G., Münnich, K. O.: Oxygen

1052   18 and Helium as tracers of ice shelf water and water/ice interactions in the Weddell Sea,

1053   J. of Geophys. Res., 95 (C3), 3253–3263, 1990.

1054 Schodlok, M. P., Menemenlis, D., Rignot, E. and Studinger, M.: Sensitivity of the ice-

1055   shelf/ocean system to the sub-ice-shelf cavity shape measured by NASA IceBridge in

1056   Pine Island Glacier, West Antarctica. Annals of Glaciology, 53(60), pp.156-162, 2012.

1057 Schoof, C.: Ice sheet grounding line dynamics: Steady states, stability, and hysteresis. J. of

1058   Geophys. Res.: Earth Surface, 112(F3), 2007.

1059 Shchepetkin, A. F., and McWilliams, J. C.: A method for computing horizontal pressure-

1060   gradient force in an oceanic model with a nonaligned vertical coordinate, J. Geophys.

1061   Res.-Ocean., 108(C3), doi:10.1029/2001JC001047, 2003.

1062 Shchepetkin, A. F., and McWilliams, J. C.: Correction and commentary for "Ocean

1063   forecasting in terrain-following coordinates: Formulation and skill assessment of the

1064   regional ocean modeling system" by Haidvogel et al., J. Comp. Phys. 227, pp. 3595–

1065   3624, J. Comp. Phys., 228(24), 8985–9000, doi:10.1016/j.jcp.2009.09.002, 2009.

1066   Shepherd et al.: A Reconciled Estimate of Ice-Sheet Mass Balance, Science, 338, 1183-

1067   1189, doi: 10.1126/science.1228102, 2012.

1068   Sutterley, T. C., Velicogna, I., Rignot, E., Mouginot, J., Flament, T., van den Broeke, M. R.,

1069   van Wessem, J. M., and Reijmer, C. H.: Mass loss of the Amundsen Sea Embayment of

1070   West Antarctica from four independent techniques, Geophys. Res. Lett., 41, 8421–8428,

1071   doi:10.1002/2014GL061940, 2014.

1072   Timmermann, R., et al.: A consistent dataset of Antarctic ice sheet topography, cavity

1073   geometry, and global bathymetry, Earth System Science Data, 2, 261–273,

1074   doi:10.5194/essd-2-261-2010, 2010.

1075   Timmermann, R., Wang, Q., and Hellmer, H. H.: Ice-shelf basal melting in a global finite-

1076   element sea-ice/ice-shelf/ocean model, Ann. Glaciol., 53 (60), 303–314,

1077   doi:10.3189/2012AoG60A156, 2012.

1078   Timmermann, R. and Hellmer, H. (2013): Southern Ocean warming and increased ice shelf

1079   basal melting in the twenty-first and twenty-second centuries based on coupled ice-ocean

1080   finite-element modelling , Ocean Dynamics, 63 (9), pp. 1011–1026 . doi:

1081   10.1007/s10236-013-0642-0.

1082   Walker, R. T., Dupont, T. K., Parizek, B. R., and Alley, R. B.: Effects of basal-melting

1083   distribution on the retreat of ice-shelf grounding lines, Geophys. Res. Lett., 350, L17503,

1084   doi:10.1029/2008GL034947, 2008.

1085   Wang, Y., Ding, M., van Wessem, J.M., Schlosser, E. , Altnau, S. , van den Broeke, M.R.,

1086   Lenaerts, J.T., Thomas, E.R., Isaksson, E., Wang, J., Sun, W.: A Comparison of

1087   Antarctic Ice Sheet Surface Mass Balance from Atmospheric Climate Models and In Situ

1088   Observations. J. Climate, 29, 5317–5337, https://doi.org/10.1175/JCLI-D-15-0642.1,

1089   2016.

1090 Webber, B. G. M, Heywood, K. J., Stevens, D. P., Dutrieux, P., Abrahamsen, E. P., Jenkins,
1091   A., Jacobs, S. S., Ha, H. K., Lee, S. H., Kim, T. W., Mechanisms driving variability in
1092   the ocean forcing of Pine Island Glacier, Nat. Commun., 8, 14507,
1093   doi:10.1038/ncomms14507, 2017.
1094 Wright, A. P., Le Brocq, A. M., Cornford, S., Bingham, R. G., Corr, H. F. J., Ferraccioli, F.,
1095   Jordan, T. A., Payne, A. J., Rippin, D. M., Ross, N. and Siegert, M. J.: Sensitivity of the
1096   Weddell Sea sector ice streams to sub-shelf melting and surface accumulation, The
1097   Cryosphere, 8, 2119–2134, doi:10.5194/tc-8-2119-2014, 2014.

1098

1099 **Table 1 An overview of the eight model runs presented in this paper and the case name that is used to reference them. The three runs that were used as the spin-up**

1100 **solutions to initialize other runs are marked and referenced as b1, b2, and b3. The four runs that include passive dye tracers are shaded in grey. All run intervals**

1101 **provide steady state solutions as determined by the transient solutions of shelf-averaged basal melt.**

1102

#	Case Name	Run length	Averaged output period	Cavity geometry	θ_{init} (°C)	min z_{ice} (m)	max z_{ice} (m)	min wct (m)	max wct (m)
1	standard cold tide-forced	20-years	30-day	present-day	-1.9	-11	-1537	50	1210
2	standard cold no-tides	10-years	30-day	present-day	-1.9	''	''	''	''
3	standard warm tide-forced	20-years	30-day	present-day	-1.4	''	''	''	''
4	standard warm no-tides	10-years	30-day	present-day	-1.4	''	''	''	''
5	standard tides-only	30-days	2-hour	present-day	NA	''	''	''	''
6	standard cold dye (restart #1)	2-year	30-day	present-day	-1.9	''	''	''	''
8	standard warm dye (restart #3)	2-year	30-day	present-day	-1.4	''	''	''	''
9	modified warm tide-forced	20-year	30-day	melt-adjusted	-1.4	-25	-1442	52	1180
10	modified warm no-tides	10-year	30-day	melt-adjusted	-1.4	''	''	''	''
11	modified tides-only	30-days	2-hour	melt-adjusted	NA	''	''	''	''
12	modified warm dye (restart #9)	2-year	30-day	melt-adjusted	-1.4	''	''	''	''

1103

1104   **Table 2 Values for integrated mass transport (M_b, Gt a^{-1}) and FRIS-averaged basal melt rate (w_b, m a^{-1}) for**
1105   **runs shown in Fig. 6: Standard cold no-tides** (S -1.9 ⊘), **Standard cold tides-forced** (S -1.9), **Standard warm**
1106   (S -1.4 ⊘), **Standard warm tides-forced** (S -1.4), **Modified warm no-tides** (M -1.4 ⊘), **Modified warm tides**
1107   (M -1.4).

		S -1.9 ⊘	S -1.9	S -1.4 ⊘	S -1.4	M -1.4 ⊘	M -1.4
M_b (Gt a^{-1})	Net	48	47	171	239	188	221
	Melt	62	104	182	262	200	246
	Freeze	-14	-57	-11	-23	-12	-25
w_b (ma^{-1})	Net	0.14	0.14	0.49	0.69	0.54	0.63
	Melt	0.27	0.46	0.66	0.95	0.69	0.86
	Freeze	-0.12	-0.44	-0.14	-0.29	-0.20	-0.37

1108

1109

1110 **Table 3 Publication sources and abbreviations used in Fig. 3. Method of calculating melt rates is summarized as Ocean Model (OM), Standard Glaciological Method**

1111 **(GM), Ocean Observation (OO), Geophysical Tracer (GT), following the nomenclature used in Table S2 of Rignot et al. (2013) supplementary document. The time**

1112 **period of observation(s) or forcing files are listed together with source of data or model output.**

Pub. Abbr.	method	reference	time period	estimate source
TS	OM	this study	NA	numerical model
M14	GM	Moholdt et al. (2014)	2003-2009	
R13	GM	Rignot et al. (2013)	2003-2009	ICESat
			2007-2008	ALOS PALSAR
				InSAR
			1979-2010	RACMO2
				Operation IceBridge
				BEDMAP
D13	GM	Depoorter et al. (2013)	2003-2009	ICESat
			1994-2002	ERS-1
			2007-2009	ERS-2
			2007-2009	InSAR
			1979-2010	RACMO2
T12	OM	Timmermann et al. (2012)	1958-2010	FESOM model, NCEP winds (1958-2010)
M11	OM	Makinson et al. (2011)	NA	
H04	OM	Holland (2004)	1978-1997	NCEP 10-m winds

				2-m air temperature
				specific humidity
				cloudiness
				and net precipitation
JP03	GM	Joughin and Padman (2003)	1997	RADARSAT InSAR
N03	OO	Nicholls et al. (2003)	1995-1999	CTD
F01	OO	Foldvik et al. (2001)	1992-1993	CTD & mooring
G99	OM	Gerdes et al. (1999)	NA	
G94	GT	Gammelsrød et al. (1994)	Feb. 1993	CFC-11, CFC-12, O2, Si
J92	GM	Jacobs et al. (1992)		
JD91	GM	Jenkins (1991)	1985-1988	Radar echo sounding
S90	GT	Schlosser et al. (1990)	Jan-Mar. 1985	$\partial_{18}O$, He

1113
1114

1115
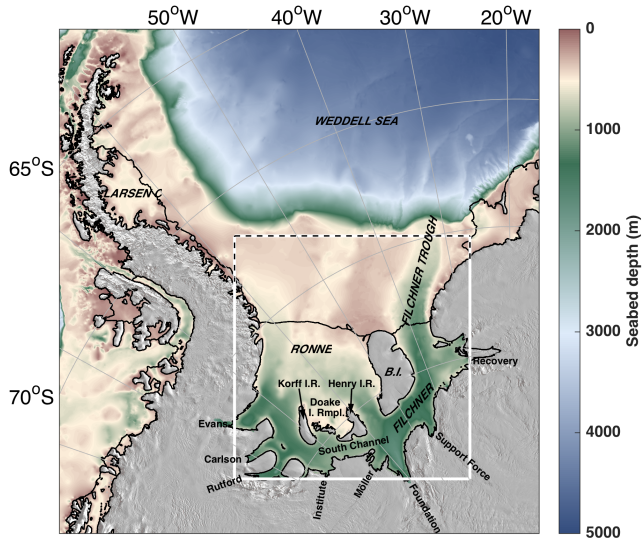
1116

Figure 1: Weddell Sea region of study with model domain outlined by white box. Dashed black lines highlight the open boundaries. The labels on land indicate the names of the tributary glaciers used for regional anslyses in this study. Black lines over seabed indicate the extend of the ice shelf and black lines around the grey mask indicate the ice sheet grounding line and/or transition between ocean and land.
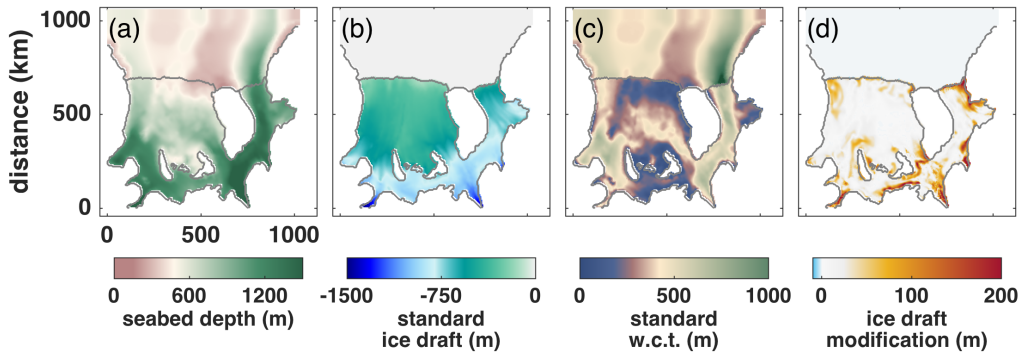
1121

Figure 2: Bathymetry (h) and ice draft (z_{ice}) for the standard and modified geometries: (a) h for both the standard and modified cases; (b) z_{ice} for the standard case; (c) $w.c.t.$ for the standard case; (d) Difference between standard z_{ice} and modified z_{ice}, where difference > 0 indicates regions of melting and a corresponding decrease in z_{ice} in the modified geometry when compared to the standard geometry.

51
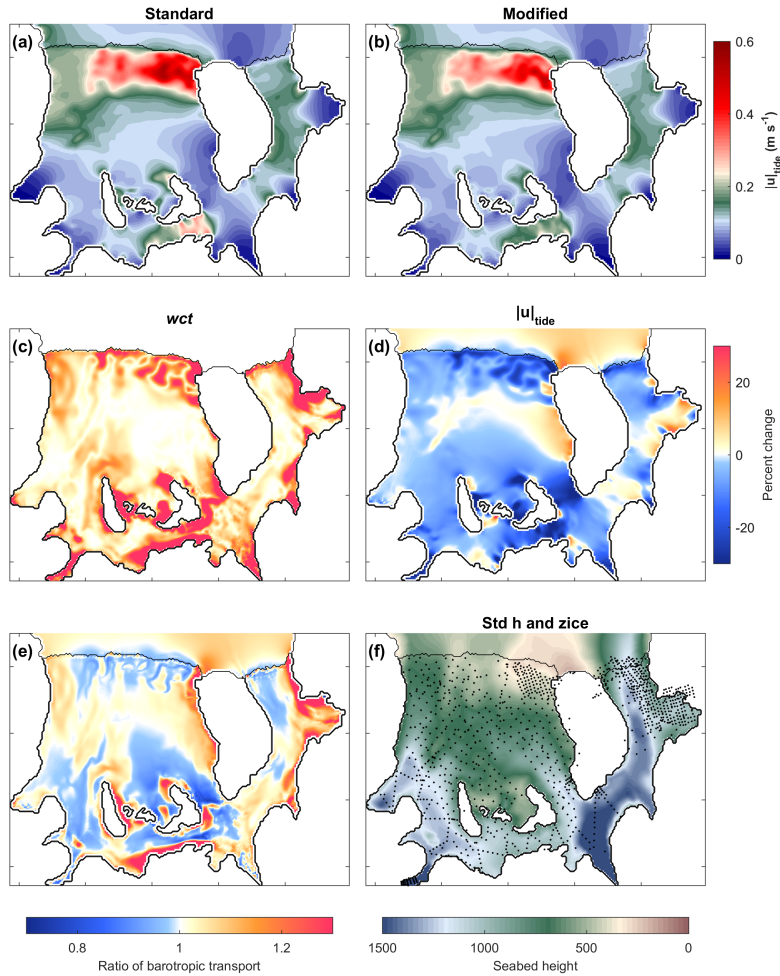
1126

Figure 3: (a) Barotropic current ($|u|_{tide}$, **Eq**. (5)) for the standard tides-only run. (b) Same as (a) but for the modified tides-only run. (c) Percent change in *wct* between the standard and modified cases with positive values indicating where the *wct* is greater in the modified geometry. (d) Change in $|u|_{tide}$ between (a) and (b) where Percent change > 0 indicates locations where the standard case $|u|_{tide}$ is greater than the modified case $|u|_{tide}$. (e) Ratio of barotropic **tidal** transport ($wct \times |u|_{tide}$) shown here as modified/standard, with values > 0 showing where there is increased transport for the modified case. (f) Seabed depth (as in Figure 2a) with existing seismic observation locations shown as black dots.

1134

52
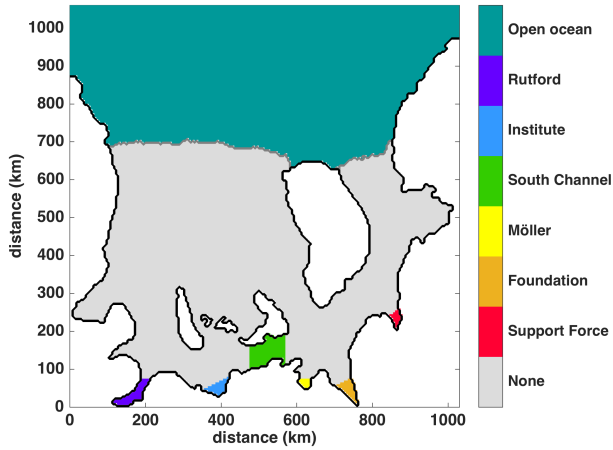
1135

1136   **Figure 4: Locations of the six, continuous, modeled meltwater dye releases and the open ocean bulk dye explained in**
1137   **Sec. 2.3.3.**
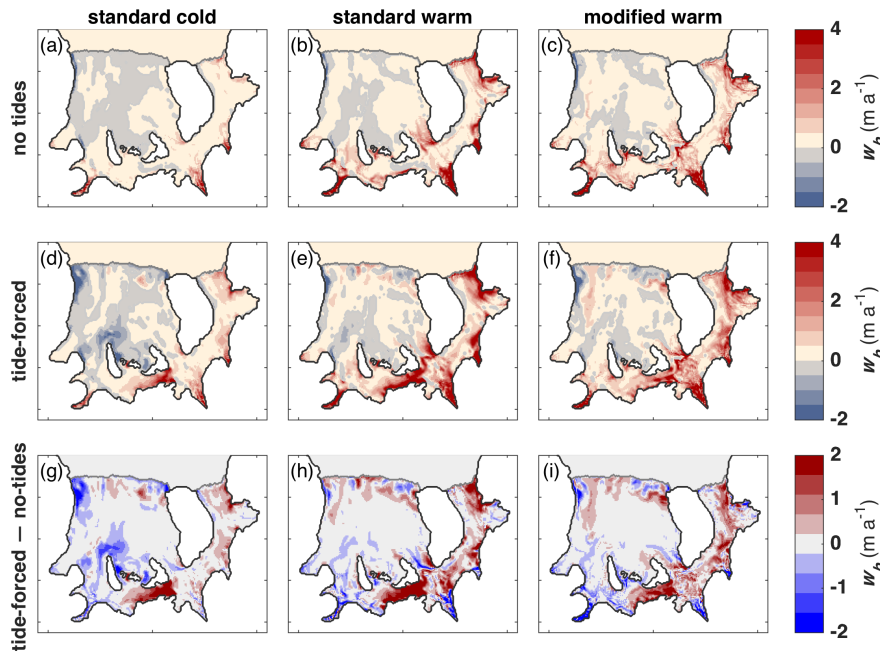
1138

1139   **Figure 5: Melt rates averaged over 1-year of steady state solutions for (top) no tides runs, (middle) tide-forced runs,**
1140   **and (bottom) the difference between the tide-forced and no-tides melt solutions. Positive values in the bottom**
1141   **subplots show where there is more basal melting in the solutions that include tidal forcing (middle subplots). The left**

1142 column (a, d, g) shows results for the standard cold case; the middle column (b, e, h) shows results for the standard
1143 warm case; and the right column (c, f, i) shows results for the modified warm case.
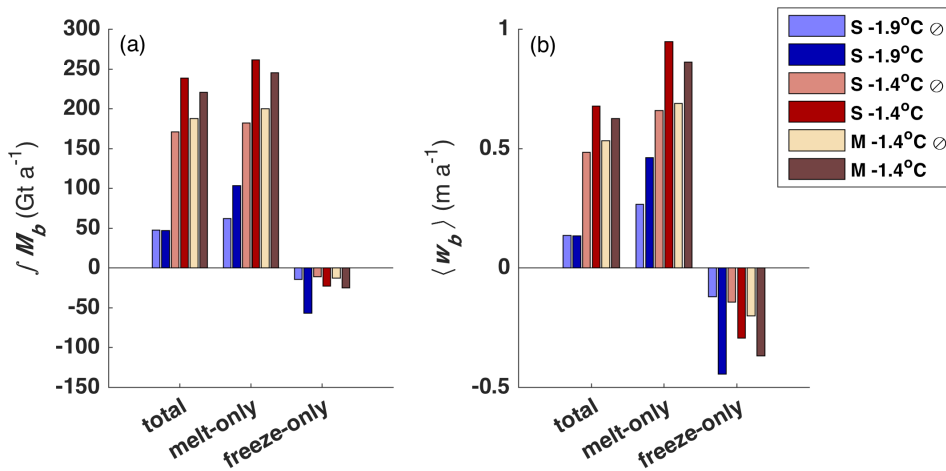
1144

1145 Figure 6: (a) integrated mass flux over "total" FRIS area, "melt-only" regions, and "freeze-only" regions for both
1146 no-tide (⊘) and tide-forced cases. (b) Same regions and runs as in (a) but showing FRIS-averaged basal melting.
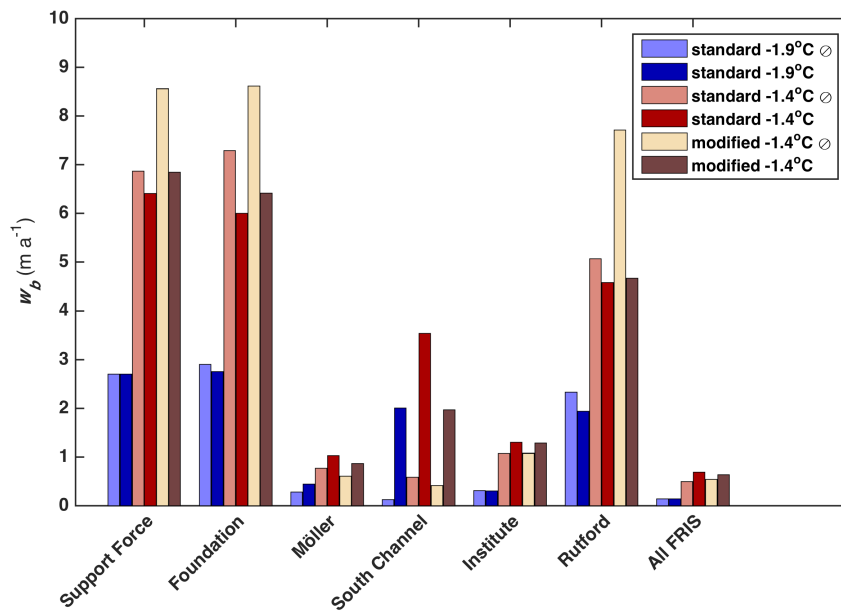
1147

1148 Figure 7: Melt rates averaged over last 12 months of steady state solutions in the standard cold, standard warm, and
1149 modified warm cases for some of the regions shown in Fig. 4 and for both no-tides (⊘) and tide-forced simulations.
1150 "All FRIS" duplicates the information shown by "total" in Fig. 6b.
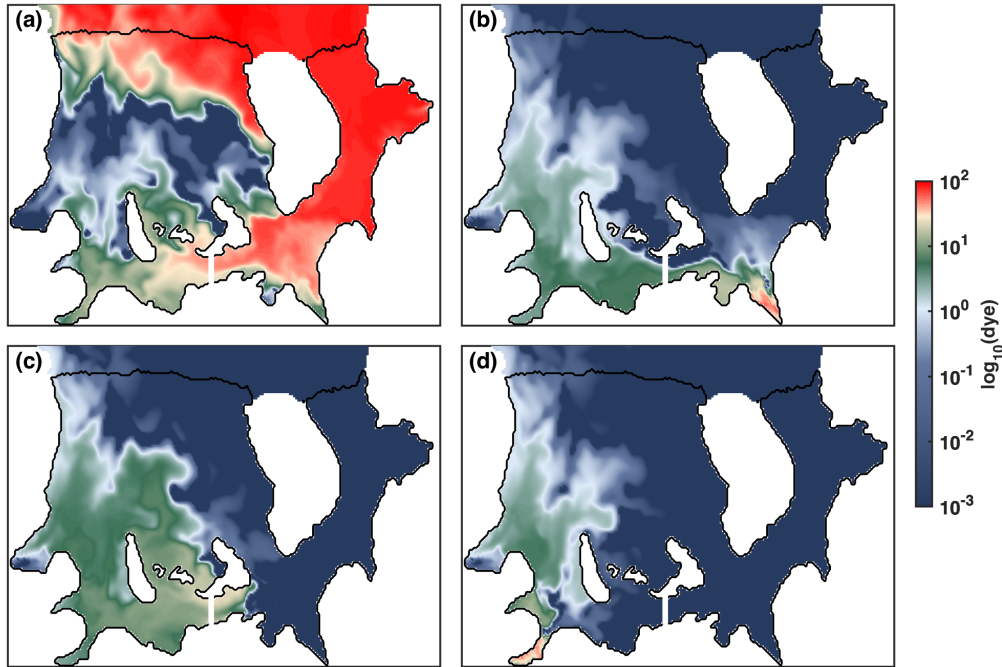
1151

Figure 8: Distribution of dye concentration from the last time step and the upper model layer of the standard cold, tide-forced case described in Sect. 2.3.3. These distributions are from 2-years after the initiation of model dye releases following 20-year of model circulation spin-up time. (a) bulk dye representing penetration of water initially north of the FRIS ice front. (b-d) meltwater dyes with sources in Foundation, South Channel, and Rutford regions, respectively (see Fig. 4 for dye release regions). The white line across South Channel represents the location of the transects in Fig. 13.
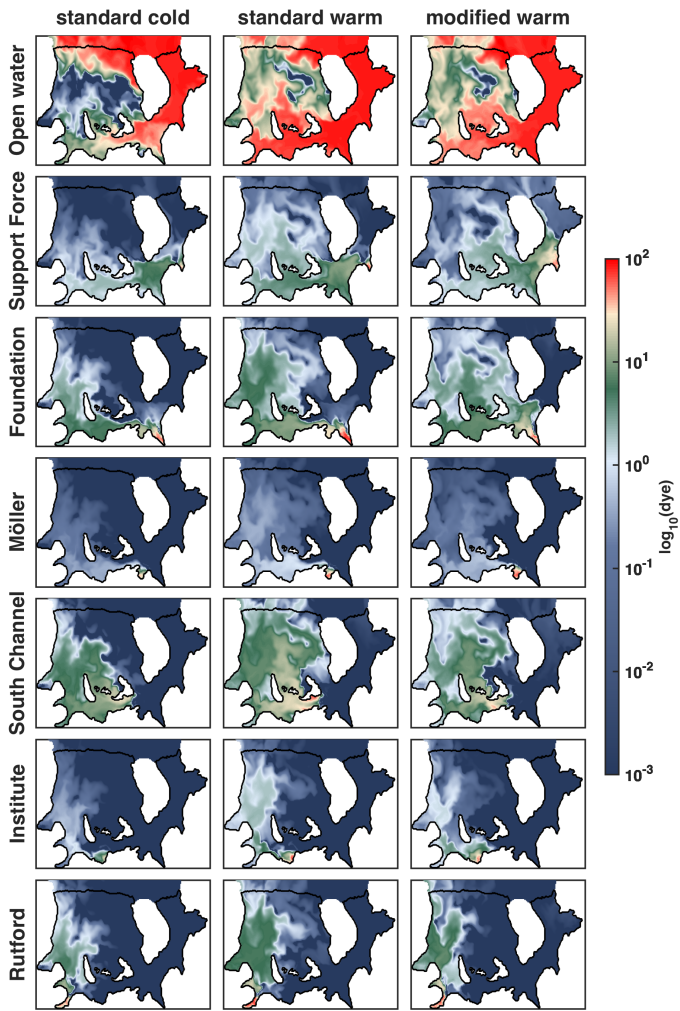
1158

1159 **Figure 9: An expanded distribution of dye concentration than that shown in Fig. 8 to include all meltwater dyes in**
1160 **the three tide-forced base simulations. As in Fig. 8, dye concentrations are from the last 30-day average of upper**
1161 **model layer solutions from the runs described in Sect. 2.3.3.** **These distributions are from 2-years after initializing**
1162 **dye release following 20-years of model circulation spin-up time.** **The left hand column of this graphic includes the**
1163 **same four regional plots as shown in Fig. 8.**

1164
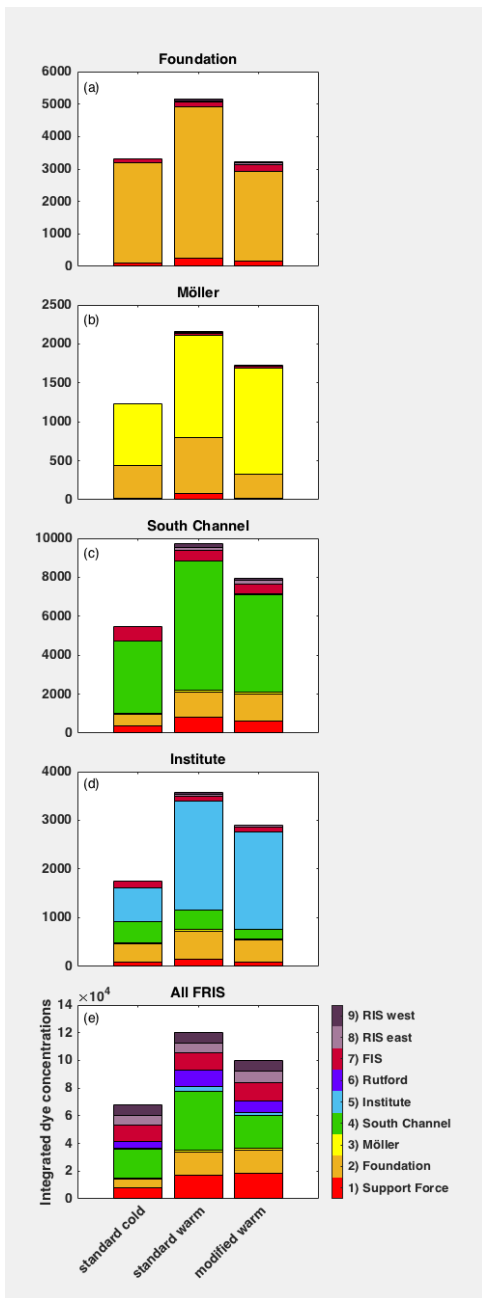
1165

Figure 10 Integrated meltwater dye (Sect. 2.3.3) by region for the tide-forced, base simulations, showing: (a) Foundation region, (b) Möller region, (c) South Channel region, (d) Institute region, and (e) all of FRIS. Regions are shown in Fig. 4.
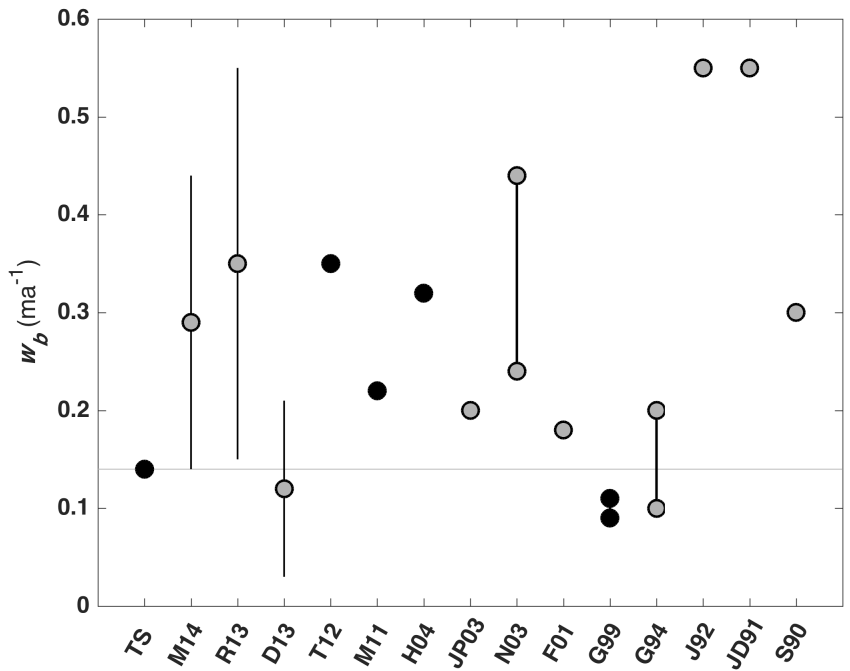
1169

Figure 11 FRIS-averaged basal melt rate comparison between this study [TS] and others. Model results are shown as black dots while observations are shown as grey dots. Error bars for remote sensing observations are shown as black lines for M14 (Moholdt et al., 2014), R13 (Rignot et al., 2013) and D13 (Depoorter et al., 2013). Min and max values are connected by thick, solid, black lines to show the range of values reported by N03 (Nicholls et al., 2003) and G94 (Gammelsrød et al., 1994). A summary of the studies presented here and their abbreviations is provided in Table 2.
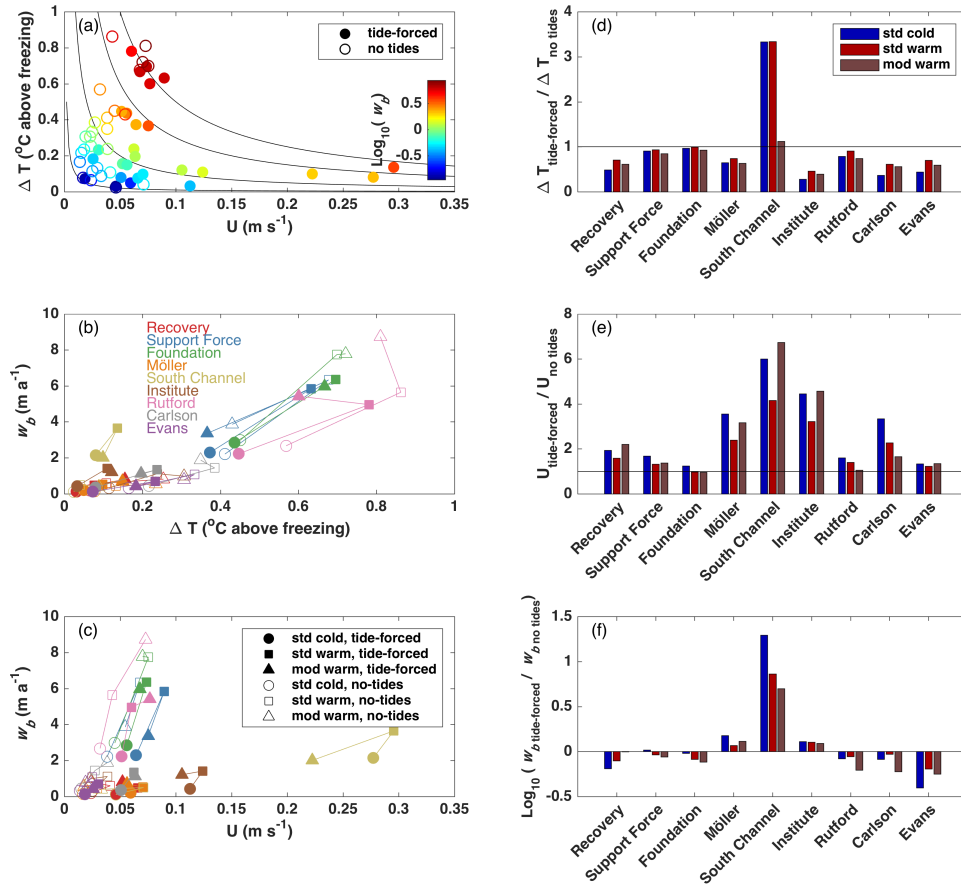
1176

Figure 12: **Regional influences of ΔT and current speed on melt rates. Tide-forced cases are plotted using solid marker style, e.g. "■", and no-tide cases are plotted using open marker style, e.g. "□". (a) Current speed (U, Eq. (6)) vs. thermal forcing (ΔT), color-coded according to melt rate (w_b). Black contours follow $\Delta T = c/U$ (with c being a set of different scalars), along which constant values of w_b (as in Sect. 3.2) are expected to be found. (b) ΔT vs. w_b for each region. (c) U vs. w_b for each region. (d) ΔT difference between no-tides and tide-forced cases such that positive values show where thermal forcing is stronger in the no-tides cases, (e) current speed difference between tide-forced (U_{tides}) and no-tides ($U_{no\,tides}$) cases, and (f) w_b difference between tide-forced and no-tides cases.**

59
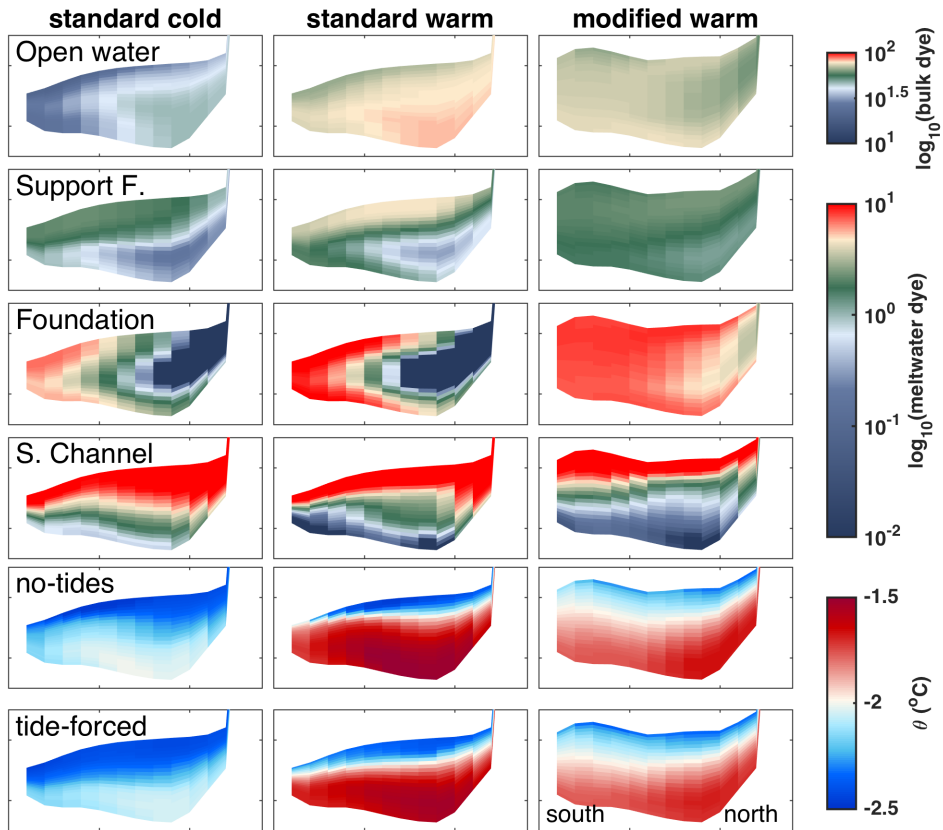
1184

Figure 13: Transects of dyes (upper four rows) and potential temperature (θ, lower two rows) across South Channel at the western tip of Henry Ice Rise. The upper four panels are for tide-forced runs only. Transect location is shown in Fig. 8.